

This is a repository copy of *Transcription factor clusters regulate genes in eukaryotic cells*.

White Rose Research Online URL for this paper:

<https://eprints.whiterose.ac.uk/id/eprint/121854/>

Version: Accepted Version

Article:

Wollman, Adam orcid.org/0000-0002-5501-8131, Shashkova, Sviatlana, Hedlund, Erik Goran et al. (3 more authors) (2017) Transcription factor clusters regulate genes in eukaryotic cells. eLife. e27451. ISSN: 2050-084X

<https://doi.org/10.7554/eLife.27451>

Reuse

This article is distributed under the terms of the Creative Commons Attribution (CC BY) licence. This licence allows you to distribute, remix, tweak, and build upon the work, even commercially, as long as you credit the authors for the original work. More information and the full terms of the licence here:

<https://creativecommons.org/licenses/>

Takedown

If you consider content in White Rose Research Online to be in breach of UK law, please notify us by emailing eprints@whiterose.ac.uk including the URL of the record and the reason for the withdrawal request.

1 **Title: Transcription factor clusters regulate genes in eukaryotic cells**

3 **Authors:**

4 Adam J. M. Wollman^{a,1}, Sviatlana Shashkova^{a,b,1}, Erik G. Hedlund^a, Rosmarie Friemann^b,
5 Stefan Hohmann^{b,c}, Mark C. Leake^{a,2}

6 **Affiliations:**

7 ^a Biological Physical Sciences Institute, University of York, York YO10 5DD, UK

8
9 ^b Department of Chemistry and Molecular Biology, University of Gothenburg, 40530
10 Göteborg, Sweden.

11
12 ^c Department of Biology and Biological Engineering, Chalmers University of Technology,
13 41296 Göteborg, Sweden.

14
15 ¹ A.J.M.W. and S.S. contributed equally to this work.

16
17 ² To whom correspondence should be addressed. Email: mark.leake@york.ac.uk.

18
19 Corresponding author: Prof Mark Leake, Biological Physical Sciences Institute, University of
20 York, York YO10 5DD, UK. Tel: +44 (0)1904322697. Email: mark.leake@york.ac.uk. Orcid
21 ID: <http://orcid.org/0000-0002-1715-1249>.

22
23 **Keywords:** gene expression; transcription factors; single-molecule; super-resolution; cell
24 signaling.

Abstract

Transcription is regulated through binding factors to gene promoters to activate or repress expression, however, the mechanisms by which factors find targets remain unclear. Using single-molecule fluorescence microscopy, we determined *in vivo* stoichiometry and spatiotemporal dynamics of a GFP tagged repressor, Mig1, from a paradigm signaling pathway of *Saccharomyces cerevisiae*. We find the repressor operates in clusters, which upon extracellular signal detection, translocate from the cytoplasm, bind to nuclear targets and turnover. Simulations of Mig1 configuration within a 3D yeast genome model combined with a promoter-specific, fluorescent translation reporter confirmed clusters are the functional unit of gene regulation. *In vitro* and structural analysis on reconstituted Mig1 suggests that clusters are stabilized by depletion forces between intrinsically disordered sequences. We observed similar clusters of a co-regulatory activator from a different pathway, supporting a generalized cluster model for transcription factors that reduces promoter search times through intersegment transfer while stabilizing gene expression.

Introduction

Cells respond to their environment through gene regulation involving protein transcription factors. These proteins bind to DNA targets of a few tens of base pairs (bp) length inside ~500-1,000bp promoter sequences to repress/activate expression, involving single (1) and multiple (2) factors, resulting in the regulation of target genes. The mechanism for finding targets in a genome ~six orders of magnitude larger is unclear since free diffusion followed by capture is too slow to account for observed search times (3). Target finding may involve heterogeneous mobility including nucleoplasmic diffusion, sliding and hops along DNA up to ~150bp, and even longer jumps separated by hundreds of bp called intersegment transfer (4–6).

In eukaryotes, factor localization is dynamic between nucleus and cytoplasm (7). Although target binding sites in some cases are known to cluster in hotspots (8) the assumption has been that factors themselves do not function in clusters but as single molecules. Realistic simulations of diffusion and binding in the complex milieu of nuclei suggest a role for multivalent factors to facilitate intersegment transfer by enabling DNA segments to be connected by a single factor (9).

The use of single-molecule fluorescence microscopy to monitor factor localization in live cells has resulted in functional insight into gene regulation (10). Fluorescent protein reporters, in particular, have revealed complexities in mobility and kinetics in bacterial (11) and mammalian cells (12) suggesting a revised view of target finding (4).

Key features of gene regulation in eukaryotes are exemplified by glucose sensing in budding yeast, *Saccharomyces cerevisiae*. Here, regulation is achieved by factors which include the Mig1 repressor, a Zn finger DNA binding protein (13) that acts on targets including *GAL* genes (14). Mig1 is known to localize to the nucleus in response to increasing extracellular glucose (15), correlated to its dephosphorylation (16, 17). Glucose sensing is particularly valuable for probing gene regulation since the activation status of factors such as Mig1 can be controlled reproducibly by varying extracellular glucose. Genetic manipulation of the regulatory machinery is also tractable, enabling native gene labeling with fluorescent reporters for functioning imaging studies.

We sought to explore functional spatiotemporal dynamics and kinetics of gene regulation in live *S. cerevisiae* cells using its glucose sensing pathway as a model for signal transduction. We used single-molecule fluorescence microscopy to track functional transcription factors with millisecond sampling to match the mobility of individual

molecules. We were able to quantify composition and dynamics of Mig1 under physiological and perturbed conditions which affected its possible phosphorylation state. Similarly, we performed experiments on a protein called Msn2, which functions as an activator for some of Mig1 target genes (18) but controlled by a different pathway. By modifying the microscope we were also able to determine turnover kinetics of transcription factors at their nuclear targets.

The results, coupled to models we developed using chromosome structure analysis, indicated unexpectedly that the functional component which binds to promoter targets operates as a cluster of transcription factor molecules with stoichiometries of ~6-9 molecules. We speculated that these functional clusters in live cells were stabilized through interactions of intrinsically disordered sequences facilitated through cellular depletion forces. We were able to mimic those depletion forces in *in vitro* single-molecule and circular dichroism experiments using a molecular crowding agent. Our novel discovery of factor clustering has a clear functional role in facilitating factors finding their binding sites through intersegment transfer, as borne out by simulations of multivalent factors (9); this addresses a long-standing question of how transcription factors efficiently find their targets. This clustering also functions to reduce off rates from targets compared to simpler monomer binding. This effect improves robustness against false positive detection of extracellular chemical signals, similar to observations for the monomeric but multivalent bacterial LacI repressor (4). Our findings potentially reveal an alternative eukaryotic cell strategy for gene regulation but using an entirely different structural mechanism.

Results

Single-molecule imaging reveals *in vivo* clusters of functional Mig1

To explore the mechanisms of transcription factor targeting we used millisecond Slimfield single-molecule fluorescence imaging (19–21) on live *S. cerevisiae* cells (Figure. 1A and Figure. 1 – Figure Supplement 1). We prepared a genomically encoded green fluorescent protein (GFP) reporter for Mig1 (Table 1). To enable nucleus and cell body identification we employed mCherry on the RNA binding nuclear protein Nrd1. We measured cell doubling times and expression to be the same within experimental error as the parental strain containing no fluorescent protein (Figure. 1 – Figure Supplement 2A). We optimized Slimfield for single-molecule detection sensitivity with an *in vitro* imaging assay of surface-immobilized purified GFP (22) indicating a brightness for single GFP molecules of ~5,000 counts on our camera detector (Figure. 1 – Figure Supplement 2B). To determine any fluorescent protein maturation effects we performed cell photobleaching while expression of any additional fluorescent protein was suppressed by antibiotics, and measured subsequent recovery of cellular fluorescence <15% for fluorescent protein components, corrected for any native autofluorescence, over the timescale of imaging experiments (Figure. 1 – Figure Supplement 2C and D).

Under depleted (0%)/elevated (4%) extracellular glucose (-/+), we measured cytoplasmic and nuclear Mig1 localization bias respectively, as reported previously (15), visible in individual cells by rapid microfluidic exchange of extracellular fluid (Figure. 1B), with high cell-cell variability (Figure. 1B middle panel). However, our ultrasensitive imaging resolved two novel components under both conditions consistent with a diffuse monomer pool and distinct multimeric foci which could be tracked up to several hundred milliseconds (Figure. 1C and Figure Supplement 3; Video 1 and 2). We wondered if the presence of foci was an artifact due to GFP oligomerization. To discourage artifactual aggregation we

performed a control using another type of GFP containing an A206K mutation (denoted GFPmut3 or mGFP) known to inhibit oligomerization (23). However, both *in vitro* experiments using purified GFP and mGFP (Figure. 1 – Figure Supplement 2B) and live cell experiments at *glucose* (-/+) (Figure. 1 – Figure Supplement 2E and F) indicated no significant difference to foci brightness values (Student's t-test, $p=0.67$). We also developed a genomically encoded Mig1 reporter using green-red photoswitchable fluorescent protein mEos2 (24). Super-resolution stochastic optical reconstruction microscopy (STORM) from hundreds of individual photoactivated tracks indicated the presence of foci, clearly present in nuclei hotspots in live cells at *glucose* (+) (Figure. 1 – Figure Supplement 1). These results strongly argue that foci formation is not dependent on hypothetical fluorescent protein oligomerization.

We implemented nanoscale tracking based on automated foci detection which combined iterative Gaussian masking and fitting to foci pixel intensity distributions to determine the spatial localization to a lateral precision of 40nm (25, 26). Tracking was coupled to stoichiometry analysis using single GFP photobleaching of foci tracks (22) and single cell copy number quantification (27). These methods enabled us to objectively quantify the number of Mig1 molecules associated with each foci, its effective microscopic diffusion coefficient D and spatiotemporal dynamics in regards to its location in the cytoplasm, nucleus or translocating across the nuclear envelope, as well as the copy number of Mig1 molecules associated with each subcellular region and in each cell as a whole. These analyses indicated ~850-1,300 Mig1 total molecules per cell, dependent on extracellular glucose. Quantitative PCR and previous work suggest a higher Mig1 copy number at *glucose* (-) (27) (Figure. 1D; Table 2 and 3).

At *glucose* (-) we measured a mean ~950 Mig1 molecules per cell in the cytoplasmic pool (Figure. 1D) and 30-50 multimeric foci in total per cell, based on interpolating the observed number of foci in the microscope's known depth of field over the entirety of the cell volume. These foci had a mean stoichiometry of 6-9 molecules and mean D of $1-2\mu\text{m}^2/\text{s}$, extending as high as $6\mu\text{m}^2/\text{s}$. In nuclei, the mean foci stoichiometry and D was the same as the cytoplasm to within experimental error (Student's t-test, $p>0.05$, $p=0.99$ and $p=0.83$), with a similar concentration. Trans-nuclear foci, those entering /leaving the nucleus during observed tracking, also had the same mean stoichiometry and D to cytoplasmic values to within experimental error ($p>0.05$, $p=0.60$ and $p=0.79$). However, at *glucose* (+) we measured a considerable increase in the proportion of nuclear foci compared to *glucose* (-), with up to 8 foci per nucleus of mean apparent stoichiometry 24-28 molecules, but D lower by a factor of 2, and 0-3 cytoplasmic/trans-nuclear foci per cell (Figure. 2A and 2B and Figure Supplement 3).

Mig1 cluster localization is dependent on phosphorylation status

To understand how Mig1 clustering was affected by its phosphorylation we deleted the *SNF1* gene which encodes the Mig1-upstream kinase, Snf1, a key regulator of Mig1 phosphorylation. Under Slimfield imaging this strain indicated Mig1 clusters with similar stoichiometry and D as for the wild type strain at *glucose* (+), but with a significant insensitivity to depleting extracellular glucose (Figure. 1 – Figure Supplement 1, Figure. 2 – Figure Supplement 1A and B). We also used a yeast strain in which the kinase activity of Snf1 could be controllably inhibited biochemically by addition of cell permeable PP1 analog 1NM-PP1. Slimfield imaging indicated similar results in terms of the presence of Mig1 clusters, their stoichiometry and D , but again showing a marked insensitivity towards depleted extracellular glucose indistinguishable from the wild type *glucose* (+) phenotype

(Figure. 1 - Figure Supplement 1, Figure. 2 – Figure Supplement 1C, Figure. 2 – Figure Supplement 2,3 and Table 4). We also tested a strain containing Mig1 with four serine phosphorylation sites (Ser222, 278, 311 and 381) mutated to alanine, which were shown to affect Mig1 localization and phosphorylation dependence on extracellular glucose (28). Slimfield showed the same pattern of localization as the *SNF1* deletion while retaining the presence of Mig1 clusters (Figure. 2 – Figure Supplement 1D and E). These results suggest that Mig1 phosphorylation does not affect its ability to form clusters, but does alter their localization bias between nucleus and cytoplasm.

Cytoplasmic Mig1 is mobile but nuclear Mig1 has mobile and immobile states

The dynamics of Mig1 between cytoplasm and nucleus is critically important to its role in gene regulation. We therefore interrogated tracked foci mobility. We quantified cumulative distribution functions (CDFs) for all nuclear and cytoplasmic tracks (12). A CDF signifies the probability that foci will move a certain distance from their starting point as a function of time while tracked. Here, we analyzed only the first displacement of each track to avoid bias toward slowly moving foci (12). A mixed mobility population can be modeled as the weighted sum of multiple CDFs characterized by different *D*. Cytoplasmic foci at *glucose* (+/-), and nuclear foci at *glucose* (-), were consistent with just a single mobile population (Figure. 3 – Figure Supplement 1) whose *D* of 1-2 $\mu\text{m}^2/\text{s}$ was consistent with earlier observations. However, nuclear foci at *glucose* (+) indicated a mixture of mobile and immobile components (Figure. 3A). These results, substantiated by fitting two Gamma functions to the distribution of estimated *D* (29) for *glucose* (+) nuclear foci (Figure. 3A, inset), indicate 20-30% of nuclear foci are immobile, consistent with a DNA-bound state. Mean square displacement analysis of foci tracks sorted by stoichiometry indicated Brownian diffusion over short timescales of a few tens of ms but increasingly anomalous diffusion over longer timescales >30ms (Figure. 3B). These results are consistent with *glucose* (+) Mig1 diffusion being impacted by interactions with nuclear structures, similar to that reported for other transcription factors (30). Here however this interaction is dependent on extracellular glucose despite Mig1 requiring a pathway of proteins to detect it, unlike the more direct detection mechanism of the prokaryotic *lac* repressor. A strain in which mCherry labeled Mig1 had its Zn finger deleted ($\Delta\text{aa}36-91$) (18) indicated no significant immobile cluster population at *glucose* (+/-) with CDF analysis (Figure. 3 – Figure Supplement 1). We conclude that Mig1 clusters bind with a relatively high association constant to the DNA via their Zn finger motif with direct glucose dependence.

Mig1 nuclear translocation selectivity does not depend on glucose but is mediated by interactions away from the nuclear envelope

Due to the marked localization of Mig1 towards nucleus/cytoplasm at *glucose* (+/-) respectively, we asked whether this spatial bias was due to selectivity initiated during translocation at the nuclear envelope. By converting trans-nuclear tracks into coordinates parallel and perpendicular to the measured nuclear envelope position, and synchronizing origins to be the nuclear envelope crossing point, we could compare spatiotemporal dynamics of different Mig1 clusters during translocation. A heat map of spatial distributions of translocating clusters indicated a hotspot of comparable volume to that of structures of budding yeast nuclear pore complexes (31) and accessory nuclear structures of cytoplasmic nucleoporin filaments and nuclear basket (32), with some nuclear impairment to mobility consistent with restrained mobility (Figure. 3C). We observed a dwell in cluster translocation

across the 30-40nm width of the nuclear envelope (Figure. 3D). At *glucose* (+) the proportion of detected trans-nuclear foci was significantly higher compared to *glucose* (-), consistent with Mig1's role to repress genes. The distribution of dwell times could be fitted using a single exponential function with ~10ms time constant similar to previous estimates for transport factors (33). However, although the relative proportion of trans-nuclear foci was much lower at *glucose* (-) compared to *glucose* (+), the dwell time constant was found to be insensitive to glucose (Figure. 3E). This insensitivity to extracellular chemical signal demonstrates, surprisingly, that there is no direct selectivity on the basis of transcription factor phosphorylation state by nuclear pore complexes themselves, suggesting that cargo selectivity mechanisms of nuclear transport (34), as reported for a range of substrates, is blind to the phosphorylation state. Coupled with our observation that Mig1 at *glucose* (-) does not exhibit significant immobility in the nucleus and that Mig1 lacking the Zn finger still accumulates in the nucleus at *glucose* (+) (Figure. 1 – Figure Supplement 1), this suggests that Mig1 localization is driven by changes in Mig1 binding affinity to other proteins, within e.g. the general corepressor complex (35), or outside the nucleus not involving the nuclear pore complex.

Mig1 nuclear foci bound to targets turn over slowly as whole clusters of ~7-9 molecules in >100s

To further understand the mechanisms of Mig1 binding/release during gene regulation we sought to quantify kinetics of these events at Mig1 targets. By modifying our microscope we could implement an independent focused laser path using the same laser source, enabling us to use fluorescence recovery after photobleaching (FRAP) to probe nuclear Mig1 turnover. The focused laser rapidly photobleached GFP content in cell nuclei in <200ms (Figure. 3F). We could then monitor recovery of any fluorescence intensity by illuminating with millisecond Slimfield stroboscopically as opposed to continuously to extend the observation timescale to >1,000s. Using automated foci detection we could separate nuclear pool and foci content at each time point for each cell. These analyses demonstrated measurable fluorescence recovery for both components, which could be fitted by single exponentials indicating fast recovery of pool at both *glucose* (-) and (+) with a time constant <5s but a larger time constant at *glucose* (+) for nuclear foci >100s (Figure. 3G). Further analysis of intensity levels at each time point revealed a stoichiometry periodicity in nuclear foci recovery equivalent to 7-9 GFP molecules (Figure. 4 – Figure Supplement 1A), but no obvious periodicity in stoichiometry measurable from pool recovery. An identical periodicity within experimental error was measured from nuclear foci at *glucose* (+) in steady-state (Figure. 4A). These periodicity values in Mig1 stoichiometry were consistent with earlier observations for cytoplasmic and trans-nuclear clusters at *glucose* (+/-), and in the nucleus at *glucose* (-), with mean stoichiometry ~7 molecules. These data taken as a whole clearly suggest that molecular turnover at nuclear foci of Mig1 bound to its target genes occurs in units of single clusters, as opposed to single Mig1 monomers.

Mig1 clusters are spherical, a few tens of nm wide

Our observations from stoichiometry, dynamics and kinetics, which supported the hypothesis that functional clusters of Mig1 perform the role of gene regulation, also suggested an obvious prediction in terms of the size of observed foci: the physical diameter of a multimeric cluster should be larger than that of a single Mig1 monomer. We therefore sought to quantify foci widths from Slimfield data by performing intensity profile analysis on background-

corrected pixel values over each foci image. The diameter was estimated from the measured width corrected for motion blur due to particle diffusion in the sampling time of a single image frame, minus that measured from single purified GFP molecules immobilized to the coverslip surface in separate *in vitro* experiments. This analysis revealed diameters of 15-50nm at *glucose* (-), which showed an increase with foci stoichiometry S that could be fitted with a power law dependence S^a (Figure. 4 – Figure Supplement 1B) with optimized exponent a of 0.32 ± 0.06 (\pm SEM). Immuno-gold electron microscopy of fixed cells probed with anti-GFP antibody confirmed the presence of GFP in 90nm cryosections with some evidence of clusters containing up to 7 Mig1 molecules (Figure. 4 – Figure Supplement 1C), however, the overall labeling efficiency was relatively low with sparse labelling in the nucleus in particular, possibly as a consequence of probe inaccessibility, resulting in relatively poor statistics. A heuristic tight packing model for GFP labeled Mig1 monomers in each cluster predicts that, in the instance of an idealized spherical cluster, $a = 1/3$. Our data at *glucose* (-) thus supports the hypothesis that Mig1 clusters have a spherical shape. For nuclear foci at *glucose* (+) we measured larger apparent diameters and stoichiometries, consistent with >1 individual Mig1 cluster being separated by less than our measured ~200nm optical resolution limit. This observation agrees with earlier measurements of stoichiometry periodicity for nuclear foci at *glucose* (+). In other words, that higher apparent stoichiometry nuclear foci are consistent with multiple individual Mig1 clusters each containing ~7 molecules separated by a nearest neighbor distance <200nm and so detected as a single fluorescent foci.

Clusters are stabilized by depletion forces

Since we observed Mig1 clusters in live cells using Slimfield imaging we wondered if these could be detected and further quantified using other methods. However, native gel electrophoresis on extracts from Mig1-GFP cells (Figure. 4 – Figure Supplement 2A) indicated a single stained band for Mig1, which was consistent with denaturing SDS-PAGE combined with western blotting using recombinant Mig1-GFP, and protein extracts from the parental cells which included no fluorescent reporter (Figure. 4 – Figure Supplement 2B and C). Slimfield imaging on purified Mig1-GFP *in vitro* under identical imaging conditions for live cells similarly indicated monomeric Mig1-GFP foci in addition to a small fraction of brighter foci which were consistent with predicted random overlap of monomer images. However, on addition of low molecular weight polyethylene glycol (PEG) at a concentration known to mimic small molecule ‘depletion’ forces in live cells (36) we detected significant numbers of multimeric foci (Figure. 4B and Figure Supplement 2D). Depletion is an entropic derived attractive force which results from osmotic pressure between particles suspended in solution that are separated by distances short enough to exclude other surrounding smaller particles. Purified GFP alone under identical conditions showed no such effect (Figure. 4 – Figure Supplement 2E). These results support a hypothesis that clusters are present in live cells regardless of the concentration of extracellular glucose, which are stabilized by depletion components that are lost during biochemical purification.

Chromosome structure modeling supports a cluster binding hypothesis

We speculated that Mig1 cluster-mediated gene regulation had testable predictions in regards to the nuclear location of Mig1 at elevated extracellular glucose. We therefore developed quantitative models to simulate the appearance of realistic images of genome-bound Mig1-GFP at *glucose* (+). We used sequence analysis to infer locations of Mig1 binding sites in the

yeast genome, based on alignment matches to previously identified 17bp Mig1 target patterns (37) which comprised conserved AT-rich 5bp and GC-rich 6bp sequences. In scanning the entire *S. cerevisiae* genome we found >3,000 hits though only 112 matches for likely gene regulatory sites located in promoter regions (Table 5). We mapped these candidate binding sites onto specific 3D locations (Figure. 4C) obtained from a consensus structure for budding yeast chromosomes based on 3C data (38). We generated simulated images, adding experimentally realistic levels of signal and noise, and ran these synthetic data through the same tracking software as for experimental data. We used identical algorithm parameters throughout and compared these predictions to the measured experimental stoichiometry distributions.

In the first instance we used these locations as coordinates for Mig1 monomer binding, assuming that just a single Mig1 molecule binds to a target. Copy number analysis of Slimfield data (Table 2) indicated a mean ~190 Mig1 molecules per cell associated with nuclear foci, greater than the number of Mig1 binding sites in promoter regions. We assigned 112 molecules to target promoter binding sites, then assigned the remaining 78 molecules randomly to non-specific DNA coordinates of the chromosomal structure. We included the effects of different orientations of the chromosomal structure relative to the camera by generating simulations from different projections and included these in compiled synthetic datasets.

We then contrasted monomer binding to a cluster binding model, which assumed that a whole cluster comprising 7 GFP labeled Mig1 molecules binds a single Mig1 target. Here we randomly assigned the 190 Mig1 molecules into just 27 (i.e. ~190/7) 7-mer clusters to the set of 112 Mig1 target promoter sites. We also implemented improvements of both monomer and cluster binding models to account for the presence of trans-nuclear tracks. Extrapolating the number of detected trans-nuclear foci in our microscope's depth of field over the whole nuclear surface area indicated a total of ~130 Mig1 molecules at *glucose* (+) inside the nucleus prior to export across the cytoplasm. We simulated the presence of these trans-nuclear molecules either using 130 GFP-labeled Mig1 molecules as monomers, or as 18 (i.e. ~130/7) 7-mer clusters at random 3D coordinates over the nuclear envelope surface (Figure. 4 – Figure Supplement 3).

We discovered that a cluster binding model which included the presence of trans-nuclear foci generated excellent agreement to the experimental foci stoichiometry distribution ($R^2=0.75$) compared to a very poor fit for a monomer binding model ($R^2<0$) (Figure. 4D). The optimized cluster model fit involved on average ~25% of promoter loci to be bound across a population of simulated cells by a 7-mer cluster with the remaining clusters located non-specifically, near the nuclear envelope, consistent with nuclear transit. This structural model supports the hypothesis that the functional unit of Mig1-mediated gene regulation is a cluster of Mig1 molecules, as opposed to Mig1 acting as a monomer.

The activator Msn2 also forms functional clusters

We wondered if the discovery of transcription factor clusters was unique to specific properties of the Mig1 repressor, as opposed to being a more general feature of other Zn finger transcription factors. To address this question we prepared a genomically encoded GFP fusion construct of a similar protein Msn2. Nrd1-mCherry was again used as a nuclear marker (Figure. 1 – Figure Supplement 1). Msn2 acts as an activator and not a repressor, which co-regulates several Mig1 target genes but with the opposite nuclear localization response to glucose (18). On performing Slimfield under identical conditions to the Mig1-GFP strain we again observed a significant population of fluorescent Msn2 foci, which had comparable *D* and stoichiometry to those estimated earlier for Mig1 (Table 2). The key

difference with the data from the Mig1-GFP strain was that Msn2, unlike Mig1, demonstrated high apparent foci stoichiometry values and lower values of D at *glucose* (-), which was consistent with its role as an activator of the same target genes as opposed to a repressor (Figure. 5A and B). Immuno-gold electron microscopy of fixed Msn2-GFP cells confirmed the presence of GFP in 90nm cryosections with evidence for clusters of comparable diameters to Mig1-GFP (Figure. 4 – Figure Supplement 1C), but with the same technical caveats and poor statistics as reported for the Mig1-GFP dataset. These results support the hypothesis that two different eukaryotic transcription factors that have antagonist effects on the same target genes operate as molecular clusters.

To test the functional relevance of Mig1 and Msn2 clusters we performed Slimfield on a strain in which Mig1 and Msn2 were genomically labeled using mCherry and orange fluorescent protein mKO2, respectively (18). This strain also contained a plasmid with GFP labeled PP7 protein to report on nuclear mRNA expressed specifically from the glycogen synthase *GSY1* gene, whose expression can be induced by glucose starvation and is a target of Mig1 and Msn2, labelled with 24 repeats of the PP7 binding sequence (39). In switching from *glucose* (+) to (-) and observing the same cell throughout, we measured PP7 accumulating with similar localization patterns to those of Mig1 clusters at *glucose* (+) (Figure. 5C). No accumulation was observed with the mutant Mig1 lacking the Zn finger, in line with previous observations (18). We calculated the numerical overlap integral between these Mig1 and PP7 foci (Figure. 5D), indicating a high mean of ~0.95, where 1 is the theoretical maximum for 100% colocalization in the absence of noise (26). We also observed similar high colocalization between Msn2-mKO2 clusters and PP7-GFP at *glucose* (-) (Figure. 5E). These results demonstrate a functional link between the localization of Mig1 and Msn2 clusters, and the transcribed mRNA from their target genes.

Mig1 and Msn2 possess intrinsic disorder which may favor clustering

Since both Mig1 and Msn2 demonstrate significant populations of clustered molecules in functional cell strains we asked the question if there were features common to the sequences of both proteins which might explain this behavior. To address this question we used multiple sequence alignment to determine conserved structural features of both proteins, and secondary structure prediction tools with disorder prediction algorithms. As expected, sequence alignment indicated the presence of the Zn finger motif in both proteins, with secondary structure predictions suggesting relatively elongated structures (Figure. 6A). However, disorder predictions indicated multiple extended intrinsically disordered regions in both Mig1 and Msn2 sequences with an overall proportion of disordered content >50%, as high as 75% for Mig1 (Figure. 6B; Table 6). We measured a trend from a more structured region of Mig1 towards the N-terminus and more disordered regions towards the C-terminus. Msn2 demonstrated a similar bipolar trend but with the structured Zn finger motif towards the C-terminus and the disordered sequences towards the N-terminus. We then ran the same analysis as a comparison against the prokaryotic transcription factor LacI, which represses expression from genes of the *lac* operon as part of the prokaryotic glucose sensing pathway. The predicted disorder content in the case of LacI was <50%. In addition, further sequence alignment analysis predicted that at least 50% of candidate phosphorylation sites in either Mig1 or Msn2 lie within these intrinsically disordered sequences (Table 6; Figure. 6A). An important observation reported previously is that the comparatively highly structured LacI exhibits no obvious clustering behavior from similar high-speed fluorescence microscopy tracking on live bacteria (4). Intrinsically disordered proteins are known to undergo phase transitions which may enable cluster formation and increase the likelihood of binding to nucleic acids (40, 41). It has been shown that homo-oligomerization is energetically more

favorable than hetero-oligomerization (42). Moreover, symmetrical arrangement of the same protein can increase accessibility of the protein to binding partners, generate new binding sites, or increase complex specificity and diversity in general (43). We measured significant changes in circular dichroism of the Mig1 fusion construct upon addition of PEG in the wavelength range 200-230nm (Figure. 6C) known to be sensitive to transitions between ordered and intrinsically disordered states (44, 45). Since the Zn finger motif lies towards the opposite terminus to the disordered content for both Mig1 and Msn2 this may suggest a molecular bipolarity which could stabilize a cluster core while exposing Zn fingers on the surface enabling interaction with accessible DNA. This structural mechanism has analogies to that of phospholipid interactions driving micelle formation, however mediated here through disordered sequence interactions as opposed to hydrophobic forces (Figure. 6C). The prevalence of phosphorylation sites located in disordered regions may also suggest a role in mediating affinity to target genes, similar to protein-protein binding by phosphorylation and intrinsic disorder coupling (46).

Discussion

Our findings address a totally underexplored and novel aspect of gene regulation with technology that has not been available until recently. In summary, we observe that the repressor protein Mig1 forms clusters which, upon extracellular glucose detection, localize dynamically from the cytoplasm to bind to locations consistent with promoter sequences of its target genes. Similar localization events were observed for the activator Msn2 under glucose limiting conditions. Moreover, Mig1 and Msn2 oligomers colocalized with mRNA transcribed from *GSY1* gene at glucose (+/-), respectively. Our results therefore strongly support a functional link between Mig1 and Msn2 transcription factor clusters and target gene expression. The physiological role of multivalent transcription factor clusters has been elucidated through simulations (9) but unobserved until now. These simulations show that intersegmental transfer between sections of nuclear DNA was essential for factors to find their binding sites within physiologically relevant timescales and requires multivalency. Previous single-molecule studies of p53(47) and TetR(48) in human cancer cells have also suggested a role for non-specific (i.e. sequence independent) transcription factor searching along the DNA. Our findings address the longstanding question of how transcription factors find their targets in the genome so efficiently. Evidence for higher molecular weight Mig1 states from biochemical studies has been suggested previously (49). A Mig1-His-HA construct was overexpressed in yeast and cell extracts run in different glucose concentrations through sucrose density centrifugation. In western blots, a higher molecular weight band was observed, attributed to a hypothetical cofactor protein. However, no cofactor was detected and none reported to date. The modal molecular weight observed was ~four times that of Mig1 but with a wide observed distribution consistent with our mean detected cluster size of ~7 molecules. The authors only reported detecting higher molecular weight states in the nucleus in repressing conditions.

Clustering of nuclear factors has been reported previously in other systems using single-molecule techniques. In particular, RNA polymerase clustering in the nucleus has been shown to have a functional role in gene regulation through putative transcription factories (50, 51). Other nuclear protein clusters have been shown to have a functional role (52) and the Bicoid transcription factor in *Drosophila melanogaster* embryos has been shown to form clusters partially mediated by regions of intrinsic disorder (53).

Our measured turnover of genome-bound Mig1 has similar timescales to that estimated for nucleoid-bound LacI (4), but similar rates of turnover have also been observed in yeast for a DNA-bound activator (54). Faster off rates have been observed during single

particle tracking of the DNA-bound fraction of the glucocorticoid receptor (GR) transcription factor in mammalian cells, equivalent to a residence time on DNA of just 1s (12). Single GR molecules appear to bind as a homodimer complex on DNA, and slower Mig1 off rates may suggest higher order multivalency, consistent with Mig1 clusters.

Estimating nearest-neighbor distances between Mig1 promoter sites in the *S. cerevisiae* genome from the 3C model (Figure. 6D) indicates 20-30% are <50 nm, small enough to enable different DNA segments to be linked through intersegment transfer by a single cluster (6, 9). This separation would also enable simultaneous binding of >1 target (Figure. 6E). The proportion of loci separated by <50nm is also consistent with the estimated proportion of immobile foci and with the proportion of cluster-occupied sites predicted from our structural model. Such multivalency chimes with the tetrameric binding of prokaryotic LacI leading to similar low promoter off rates (4).

Measuring the variation of electrostatic charge of residues for the amino acid sequences of both Mig1 and Msn2 (Figure. 6F) we see that the regions in the vicinity of the Zn finger motifs for both proteins have a strong net positive charge compared to the rest of the molecule. If these regions project outwards from a multivalent transcription factor cluster, as per our hypothesized cluster model (Figure. 6E), then the cluster surface could interact electrostatically with the negatively charged phosphate backbone of DNA to enable a 1D sliding diffusion of the protein along a DNA strand, such that the on rate for the protein-DNA interaction is largely sequence-independent in regards to the DNA. Particular details of this type of transcription factor binding to non-specific regions of DNA have been investigated at the level of single transcription factor molecules using computational simulations (55), and suggest initial recognition is most likely via the DNA minor grooves where the phosphates are closer to each other, followed by subsequent interactions between exposed residues on the transcription factor surface and nitrogen bases. This lack of sequence dependence for binding is consistent with observations from an earlier live cell single-molecule tracking study of the TetR repressor (48). We also see experimental evidence for this in our study here, in that we find that the best fit model to account for fluorescence images of the nucleus under high glucose conditions is a combination of occupancy of clusters at the target genes (i.e. sequence specific) with random occupancy to other parts of the genome away from the target genes (i.e. sequence non-specific). Ultimate binding to the gene target once encountered could then be mediated through sequence-specific interactions via the Zn finger motif itself.

If the haploid genome of budding yeast, containing 12.1Mbp, is modeled as a flexible ‘virtual’ tube of length 4.1mm ($12.1 \times 10^6 \times 0.34\text{nm}$ for each bp separation parallel to the double helix axis of DNA) with a circular cross-section, then we can calculate that the diameter of the tube required in principle to completely occupy the volume of a typical yeast nucleus (roughly a sphere of diameter $\sim 2\mu\text{m}$) is 30-40nm. This tube diameter, in the absence of local contributions from histone packing, is thus a rough estimate for the effective average separation of DNA strands in the nucleus (i.e. the ‘mesh size’), which is very close to the diameter of clusters we observe. A multivalent transcription factor cluster thus may have only a relatively short distance to diffuse through the nucleoplasm if it dissociates from one DNA strand and then rebinds electrostatically to the next nearest strand, thereby facilitating intersegmental transfer. In this scheme, the association interaction between clusters and neighboring DNA strands is predominantly electrostatic and therefore largely, one might speculate, sequence-independent. However, sequence specificity may be relevant in generating higher-order packed structures of chromatin resulting in localized differences to the nearest neighbor separation of different DNA strands, which could therefore influence the rate at which a cluster transfers from one strand to another. In addition, there may also be localized effects of DNA topology that affect transcription factor binding, which in turn

would be expected to have some sequence specificity (55). Also, the off rates of cluster interactions with DNA may be more dependent on the specific sequence. For example, one might anticipate that the dissociation of translocating clusters would be influenced by the presence of obstacles, such as other proteins, already bound to DNA which in turn may have sequence specificity. In particular, bound RNA polymerases present during gene transcription at sequence specific sites could act as roadblocks to kick off translocating clusters from a DNA strand, to again facilitate intersegmental transfer.

Several previous experimental studies report observations consistent with intersegmental transfer relevant to our study here. For example, an investigation using single-molecule tracking indicated that transcription factor search times were increased if intersegmental transfer was specifically abrogated (56). These observations are consistent with other experiments that selectively enabled intersegmental transfer by altering DNA conformation (57, 58). Also, they are consistent with biochemical measurements that transcription factors spend a high fraction of their time bound to DNA, as opposed to being in solution (56, 59). Furthermore, other light microscopy studies report direct experimental evidence for intersegmental transfer (6, 60).

It is well-established from multiple studies that 3D diffusion of transcription factors in the nucleoplasm alone cannot account for the relatively rapid search times observed experimentally to find specific targets in the genome (3–6). Constraining the dimensionality of diffusion to just 1D, as in the sliding of weakly bound transcription factors on DNA, speeds up this process, but is limited by encountering obstacles already bound to the DNA which potentially result in dissociation of the transcription factor and then slow 3D diffusion in the nucleoplasm. In our system, we speculate that the clusters we observe can slide on DNA in a largely sequence-independent manner but then can cross to neighboring DNA strands in a process likely to have some sequence dependence when an obstacle is encountered, and thus predominantly circumvent the requirement for slow 3D diffusion in the nucleoplasm. Minimizing the contribution from the slowest component in the search process may therefore result in an overall reduction in the amount of time required for a given transcription factor to find its gene target.

Extensive bioinformatics analysis of proteome disorder across a range of species suggests a sharp increase from prokaryotes to eukaryotes (61), speculatively due to the prokaryotic absence of cell compartments and regulated ubiquitination mechanisms lowering protection of unfolded disordered structures from degradation (62). Our discovery in yeast may reveal a eukaryotic adaptation that stabilizes gene expression. The slow off rate we measure would result in insensitivity to high frequency stochastic noise which could otherwise result in false positive detection and an associated wasteful expression response. We also note that long turnover times may facilitate modulation between co-regulatory factors by maximizing overlap periods, as suggested previously for Mig1/Msn2 (18).

Our results suggest that cellular depletion forces due to crowding enable cluster formation. Crowding is known to increase oligomerization reaction rates for low association proteins but slow down fast reactions due to an associated decrease in diffusion rates, and have a more pronounced effect on higher order multimers rather than dimers (36). It is technically challenging to study depletion forces *in vivo*, however there is growing *in vitro* and *in silico* evidence of the importance of molecular crowding in cell biology. A particularly striking effect was observed previously in the formation of clusters of the bacterial cell division protein FtsZ in the presence of two crowding proteins – hemoglobin and BSA (63). Higher order decamers and multimers were observed in the presence of crowding agents and these structures are thought to account for as much as 1/3 of the *in vivo* FtsZ content.

Similarly, two recent yeast studies of the high-osmolarity glycerol (HOG) pathway also suggest a dependence on gene expression mediated by molecular crowding (64, 65).

The range of GFP labeled Mig1 cluster diameters *in vivo* of 15-50nm is smaller than the 80nm diameter of yeast nuclear pore complexes (66), not prohibitively large as to prevent intact clusters from translocating across the nuclear envelope. An earlier *in vitro* study using sucrose gradient centrifugation suggested a Stokes radius of 4.8 nm for the Mig1 fraction, i.e. diameter 9.6nm, large for a Mig1 monomer (49) whose molecular weight is 55.5kDa, e.g. that of monomeric bovine serum albumin (BSA) at a molecular weight of 66kDa is closer to 3.5nm (67). The authors ascribed this effect to a hypothetical elongated monomeric structure for Mig1. The equivalent Stokes radius for GFP has been measured at 2.4nm (68), i.e. diameter 4.8nm. Also, for our Mig1-GFP construct there are two amino acids residues in the linker region between the Mig1 and GFP sequences (i.e. additional length 0.7-0.8nm). Thus the anticipated hydrodynamic diameter of Mig1-GFP is 15-16nm. The mean observed ~7-mer cluster diameter from Slimfield data is ~30nm, which, assuming a spherical packing geometry, suggests a subunit diameter for single Mig1-GFP molecules of $\sim 30/7^{1/3} \approx 15.6\text{nm}$, consistent with that predicted from the earlier hydrodynamic expectations. Using Stokes law this estimated hydrodynamic radius indicates an effective viscosity for the cytoplasm and nucleoplasm as low as 2-3cP, compatible with earlier live cell estimates on mammalian cells using fluorescence correlation spectroscopy (FCS) (69).

One alternative hypothesis to that of intrinsically disordered sequences mediating Mig1 cluster formation is the existence of a hypothetical cofactor protein to Mig1. However, such a cofactor would be invisible on our Slimfield assay but would result in a larger measured hydrodynamic radius than we estimate from fluorescence imaging, which would be manifest as larger apparent viscosity values than those we observe. Coupled to observations of Msn2 forming clusters also, and the lack of any reported stable cofactor candidate to date, limits the cofactor hypothesis. Pull down assays do suggest that promoter bound Mig1 consists of a complex which includes the accessory proteins Ssn6 and Tup1 (35), however this would not explain the observation of Mig1 clusters outside the nucleus.

There may be other advantages in having a different strategy between *S. cerevisiae* and *E. coli* to achieve lowered transcriptional regulator off rate. A clue to these may lie in phosphorylation. We discovered that at least 50% of candidate serine or threonine phosphorylation sites in Mig1 and Msn2 lie in regions with high intrinsic disorder, which may have higher sequence-unspecific binding affinities to DNA (40, 41). Thus phosphorylation at sites within these regions may potentially disrupt binding to DNA, similar to observed changes to protein-protein affinity being coupled to protein phosphorylation state (46). Previous studies indicate that dephosphorylated Mig1 binds to its targets (70). Thus, intrinsic disorder may be required for bistability in affinity of Mig1/Msn2 to DNA.

Wide scale bioinformatics screening reveals a significant prevalence of intrinsic disorder in eukaryotic transcription factors (71). Our discovery is the first, to our knowledge, to make a link between predicted disorder and the ability to form higher-order clusters in transcription factors. Thus, our results address the longstanding question of why there is so much predicted disorder in eukaryote transcription factors. Our observations that protein interactions based on weak intracellular forces and molecular crowding has direct functional relevance may stimulate new research lines in several areas of cell biology. For example, our findings may have important mechanistic implications for other aggregation processes mediated through intrinsic disorder interactions, such as those of amyloid plaques found in neurodegenerative disorders including Alzheimer's and Parkinson's diseases (72). Increased understanding of the clustering mechanism may not only be of value in understanding such diseases, but could enable future novel synthetic biology applications to manufacture gene circuits with, for example, a range of bespoke response times.

Materials and methods

Strain construction and characterization

We developed Mig1 fluorescent protein strains based on strain YSH1351 (16) using eGFP in the first instance and also mGFP/GFPmut3 designed to inhibit oligomerization (23), and photoswitchable mEos2 (24). Mig1-mGFP and Mig1-mEos2 fusions were constructed by introducing into YSH1351 (BY4741 wild type) cells the *mGFP-HIS3* or *mEos2-HIS3* PCR fragment flanked on its 5' end with 50bp sequence of *MIG1* 3' end and 50bp downstream of *MIG1* excluding the STOP codon. The *mEos2-HIS3* and *mGFP-HIS3* fragment was amplified from mEOS-his plasmid (GeneArt, Life Technologies) and pmGFP-S plasmid designed for this study by inserting the mGFP sequence into plasmid YDp-H. Modified strains in which the *SNF1* gene was deleted, *snf1Δ*, were prepared by compromising the gene with an auxotrophic marker by providing the *LEU2* fragment amplified from plasmid YDp-L and flanked with 50bp of *SNF1* upstream and downstream sequence on 5' and 3' ends, respectively, directly into cells. Strains in which Snf1 kinase activity can be inhibited by 25μM 1NM-PP1 in DMSO were prepared by introducing into cells a plasmid with an ATP analog-sensitive version of Snf1 with *I132G* mutation (73). DMSO itself has been shown previously not to affect Mig1's behavior under different glucose conditions (17) similar to our own findings (Figure. 2 – Figure supplement 2). All transformations were performed using the lithium acetate protocol (74).

Cell doubling times of all strains were calculated (75) (Figure. 1 – Figure Supplement 2A) based on OD₆₀₀ values obtained during cultivation in media supplemented with 4% or 0.2% glucose (Bioscreen analyser C). We quantified mRNA relative expression of the *MIG1* gene using qPCR against the constitutive actin gene *ACT1* in the wild type and the Mig1-mGFP strain in cells pre-grown in 4% glucose and then shifted to elevated (4%) and depleted (0.2%) extracellular glucose for 2 h. mRNA isolation and cDNA synthesis were performed as described previously (76).

For Msn2-GFP experiments we used the YSH2350 strain (*MATa msn2-GFP-HIS3 nrd1-mCherry-hphNT1 MET LYS*) in BY4741 background.

Protein production and purification

His-tagged *mCherry*, *eGFP* and *mGFP* genes were amplified by PCR and cloned into pET vectors. An expression pRSET A plasmid containing 6xHis-Mig1-mGFP was obtained commercially (GeneArt, Life Technologies). *Escherichia coli* strain BL21(DE3) carrying the expression plasmid was grown in LB with 100μg/ml ampicillin and 34μg/ml chloramphenicol at 37°C to OD₆₀₀ 0.7. Protein expression was induced by adding isopropyl-β-D-thiogalactopyranoside (IPTG) at final concentration of 1mM for 3h at 30°C. Cells were suspended in 50mM NaH₂PO₄, 10mM Tris, 300mM NaCl, 2mM EDTA, 0.2mM PMSF, 0.1% β-mercaptoethanol, pH 8.0, and lysed by sonication or by three passages through a chilled Emulsiflex (Avestin). Extracts were cleared (24,000g, 30min) and filtered (pore diameter 0.45μm; Millipore, Bedford). All proteins were purified using Ni²⁺ affinity chromatography on a 5ml HisTrap FF column (GE Healthcare). Mig1-mGFP was eluted with a linear gradient 0 - 0.4 M imidazole in lysis buffer. Mig1-mGFP was further purified by size-exclusion chromatography (Superdex 200 Increase 10/300, GE Healthcare) and concentrated (50 kDa molecular weight cutoff VIVASPIN 20 concentrator). Purity of the sample was confirmed by Coomassie stained SDS-PAGE gels (Simply Blue Safe Stain, Life Technologies).

Media and growth conditions

Cells from frozen stocks were grown on plates with standard YPD media (10 g/l yeast extract, 20 g/l bacto-peptone, 20 g/l agar) supplemented with 4% glucose (w/v) at 30°C overnight. For the liquid cultures, the YPD was prepared as above but without agar, and the cells were grown at 30°C while shaking (180 rpm).

For transformants that carried a plasmid with mutated *SNF1* (p*SNF1-I132G*) or PP7-2xGFP (pDZ276), minimal YNB media with –URA amino acid supplement was applied. For the growth rate experiments cells were grown on 100 well plates in YNB with complete amino acid supplement and 4% glucose (w/v) until logarithmic phase, subcultured into fresh medium on a new 100 well plate and grown until logarithmic phase again. 10 µl of each culture was resuspended in 250 µl of fresh YNB medium with 4% or 0.2% glucose (w/v) on a new plate and cultivated in Bioscreen analyser C for 96 h at 30°C or 22°C. OD measurements at 600 nm were taken every 10 min with prior shaking. Each strain was represented in sextuplicates.

For microscopy experiments on the BY4741 wild type and/or cells with genetically integrated fluorescent proteins, minimal YNB media (1.7 g/l yeast nitrogen base without amino acids and (NH₄)₂SO₄, 5 g/l (NH₄)₂SO₄, 0.79 g/l complete amino acid supplement as indicated by manufacturer) with appropriate glucose concentrations was used. In brief, cells were first streaked onto YPD plates, grown overnight at 30°C prior to culturing in liquid minimal YNB media with complete amino acid supplement and 4% glucose overnight, then sub-cultured into fresh YNB with 4% glucose for 4h with shaking at 30°C. Cultures were spun at 3,000rpm, re-suspended into fresh YNB with (4%) or without (0%) glucose, immobilized in 1µl spots onto an 1% agarose well perfused with YNB minimal media with an appropriate glucose concentration enclosed between a plasma-cleaned BK7 glass microscope coverslip and slide, which permitted cells to continue to grow and divide (20, 21) while being observed for up to several hours if required. Images were acquired not longer than 2 hours after the last media switch.

SDS-PAGE

50 ml cultures of YSH1703 transformed with centromeric pMig1-HA and p*SNF1-I132G*-TAP or p*SNF1*-TAP plasmids were grown until mid-log phase in yeast nitrogen base, 4% glucose, uracil and histidine deficient. Each culture was separated into two new cultures with 4% and 0.05% glucose, respectively, and incubated for 30 min. The following procedure was adapted from Bendrioua et al (16). Cells were harvested by centrifugation (3,000rpm, 50s), suspended in 1 ml of 0.1M NaOH for 5 min and spun down. Pellets were suspended in 2 ml of 2M NaOH with 7% β- mercaptoethanol for 2 min and then 50% trichloroacetic acid was added. Samples were vortexed and spun down at 13,000rpm. The pellets were washed in 0.5 ml of 1M Tris-HCl (pH 8.0), resuspended in 50 µl of 1x SDS sample buffer (62.5 mM Tris-HCl (pH 6.8), 3% SDS, 10% glycerol, 5% β-mercaptoethanol, and 0.004% bromophenol blue) and boiled for 5 min. The protein extracts were obtained by centrifuging at the maximal speed and collecting the supernatants. For western blotting, 50 µg of extracted proteins were resolved on a Criterion TGX 10% precast polyacrylamide gel, then transferred onto a nitrocellulose membrane (Trans-Blot Turbo Transfer Pack, Bio-Rad) using Trans-Blot Turbo Transfer System (Bio-Rad). After transfer, the membrane was blocked in Odyssey Blocking buffer (LI-COR Biosciences). Mig1 was detected using primary mouse anti-HA (1:2000) antibodies (Santa Cruz), then secondary goat anti-mouse IRDye-800CW (1:5000) antibodies (LI-COR Biosciences). The result was visualized using an infrared imager (Odyssey, LI-COR Biosciences), 800nm channel.

Native PAGE

A 50 ml culture of the YSH2862 strain was grown until mid-log phase in rich media with 4% glucose, then, 25 ml of the culture was transferred into fresh YPD with 4% glucose, and the rest into YPD with 0.05% glucose for 30 min. The cultures were harvested by centrifugation, suspended in 0.1ml of solubilization buffer (100 mM Tris-HCl, pH 6.8, 0.1 mM Na₃VO₄, 1x protease inhibitor cocktail (Roche), 0.1% Triton-X100). 400µl of glass beads were added, and cells were broken by FastPrep, 6m/s, 20 s. Protein extracts were obtained by adding 150 µl of solubilization buffer, centrifugation at 13,000 rpm, 5min and collecting the supernatant. Protein quantification was performed by using Bradford with BSA standard (Bio-Rad). 250 µg of total protein extracts were run on a Criterion TGX Stain Free 10% precast polyacrylamide gel (Bio-Rad). Samples were diluted 1:1 with 2x Native Sample Buffer (Bio-Rad). Electrophoresis was performed at 4°C starting at 100V until the bromophenol blue line reached the end of the gel. The gel was transferred onto a nitrocellulose membrane (Trans-Blot Turbo Transfer Pack, Bio-Rad) using Trans-Blot Turbo Transfer System (Bio-Rad). After transfer, the membrane was blocked in Odyssey Blocking buffer (LI-COR Biosciences), analyzed by immunoblotting with mouse anti-GFP (1:500) antibodies (Roche) and visualized with goat anti-mouse IRDye-800CW (1:5,000) antibodies (LI-COR Biosciences) by using an infrared imager (Odyssey, LI-COR Biosciences), 800nm channel. As a molecular weight reference, a NativeMark Unstained Protein Standards (Invitrogen) were used.

Slimfield microscopy

A dual-color bespoke laser excitation single-molecule fluorescence microscope was used (21, 27, 77) utilizing narrow epifluorescence excitation of 10µm full width at half maximum (FWHM) in the sample plane to generate Slimfield illumination. GFP and mCherry excitation used co-aligned linearly polarized 488 nm and 561 nm wavelength 50 mW lasers (Coherent Obis) respectively which could be attenuated independently via neutral density filters followed by propagation through an achromatic $\lambda/2$ plate to rotate the plane of polarization prior to separation into two independent paths generated by splitting into orthogonal polarization components by a polarization splitting cube to enable simultaneous Slimfield illumination and a focused laser bleach illumination path for fluorescence recovery after photobleaching (FRAP) when required. The two paths were reformed into a single common path via a second polarization cube, circularized for polarization via an achromatic $\lambda/4$ plate with fast axis orientated at 45° to the polarization axes of each path and directed at ~6 W/cm² excitation intensity onto the sample mounted on an xyz nanostage (Mad City Labs) via a dual-pass green/red dichroic mirror centered at long-pass wavelength 560nm and emission filters with 25nm bandwidths centered at 525nm and 594nm (Chroma).

Fluorescence emissions were captured by a 1.49NA oil immersion objective lens (Nikon) and split into green and red detection channels using a bespoke color splitter utilizing a long-pass dichroic mirror with wavelength cut-off of 565nm prior to imaging each channel onto separate halves of the same EMCCD camera detector (iXon DV860-BI, Andor Technology, UK) at a pixel magnification of 80 nm/pixel using 5ms camera exposure time. We confirmed negligible measured crosstalk between GFP and mCherry signals to red and green channels respectively, using purified GFP and mCherry sampled in an *in vitro* surface immobilization assay (details below).

Three color microscopy was performed on the same microscope, using a 50mW 532nm wavelength laser (Obis) to excite mKO2, coupled into the same optics as before with the addition of a 532nm notch rejection filter (Semrock) in both channels of the imaging path. This allowed 1mW of laser excitation at the sample. Due to the high copy number of plasmid expressed PP7-2xGFP and the 48 RNA loci, the 488nm wavelength laser was attenuated to

~10 μ W. Each fluorophore was separately excited in the following order: mCherry, mKO2 and GFP to prevent crosstalk. mCherry and mKO2 both emit in the ‘red’ channel of the microscope, while GFP appears in the ‘green’ with very limited crosstalk.

Microfluidics control of single cell imaging

To investigate time-resolved glucose concentration-dependent changes in Mig1-GFP localization in individual yeast cells, we used bespoke microfluidics and our bespoke control software *CellBild* (LabVIEW, National Instruments), enabling cell-to-cell imaging in response to environmental glucose changes. *CellBild* controlled camera acquisition synchronized to flow-cell environmental switches via a syringe pump containing an alternate glucose environment. Microfluidic flow-chambers were based on an earlier 4-channel design (78).

Prior to each experiment flow-chambers were wetted and pre-treated for 15min with 1 mg/ml of concanavalin A (ConA) which binds to the glass surface of the plasma cleaned flow-chamber. Cells were introduced via a side channel and were left to bind ConA for 15min to immobilize cells on the surface. Any remaining ConA and unbound cells were washed out and a steady flow of YNB with 0% glucose provided to one of the central channels by gravity feed. A syringe pump synchronized with image acquisition introduced YNB with 4% glucose in the second central channel. The pumped alternate environment reaches cells within 1-2s at a flow rate of 10 μ l/min, enabling rapid change between two different glucose concentrations.

Slimfield imaging was performed on a similar bespoke microscope setup at comparable laser excitation intensities and spectral filtering prior to imaging onto a Photometrics *Evolve Delta 512* EMCCD camera at 200 frames per second. Alternating frame laser excitation (ALEX) was used to minimize any autofluorescence contamination in the red channel introduced by the blue excitation light.

Around 1-4 cells were imaged in a single field of view for each glucose exchange. The same flow chamber was used for multiple fields of view such that each cell analyzed may have experienced up to four glucose exchange cycles.

Foci detection, tracking and stoichiometry determination

Foci were automatically detected using software written in MATLAB (Mathworks) (25), lateral localization ~40nm, enabling estimates of D and stoichiometry. Our bespoke foci detection and tracking software objectively identifies candidate bright foci by a combination of pixel intensity thresholding and image transformation to yield bright pixel coordinates. The intensity centroid and characteristic intensity, defined as the sum of the pixel intensities inside a 5 pixel radius region of interest around the foci minus the local background and corrected for non-uniformity in the excitation field are determined by iterative Gaussian masking. If the signal-to-noise ratio of the foci, defined as the characteristic intensity per pixel/background standard deviation per pixel, is >0.4 it is accepted and fitted with a 2D radial Gaussian function to determine its sigma width, which our simulations indicate single-molecule sensitivity under typical *in vivo* imaging conditions (27). Foci in consecutive image frames within a single point spread function (PSF) width, and not different in brightness or sigma width by more than a factor of two, are linked into the same track. The microscopic diffusion coefficient D is then estimated for each accepted foci track using mean square displacement analysis, in addition to several other mobility parameters.

Cell and nuclear boundaries were segmented from GFP and mCherry fluorescence images respectively using a relative threshold pixel intensity value trained on simulated images of uniform fluorescence in idealized spherical compartments. An optimized threshold

value of 0.3 times the mean compartment fluorescence intensity segmented the boundary to within 0.5 pixels.

The characteristic brightness of a single GFP molecule was determined directly from *in vivo* data and corroborated using *in vitro* immobilized protein assays (22). The intensity of tracked fluorescent foci in live cells was measured over time as described above (Figure. 1–Figure Supplement 3). These followed an approximately exponential photobleach decay function of intensity with respect to time. Every oligomeric Mig1-GFP complex as it photobleaches to zero intensity will emit the characteristic single GFP intensity value, I_{GFP} , i.e. the brightness of a single GFP molecule, given in our case by the modal value of all foci intensities over time, and can potentially bleach in integer steps of this value at each sampling time point. This value of I_{GFP} was further verified by Fourier spectral analysis of the pairwise distance distribution (22) of all foci intensities which yields the same value to within measurement error in our system.

All foci tracks found within 70 image frames of the start of laser illumination were included in the analysis and were corrected for photobleaching by weighting the measured foci intensity I at a time t following the start of laser illumination with a function $\exp(+t/t_b)$ to correct for the exponential photobleach decay $I_0\exp(-t/t_b)$, of each intensity trace with a fixed time constant, where I_0 is the initial unbleached intensity. This photobleach time constant t_b was determined from exponential decay fits to the foci intensities and whole cell intensities over time to be 40 ± 0.6 ms. Stoichiometries were obtained by dividing the photobleach estimate for the initial intensity I_0 of a given foci by the characteristic single GFP molecule brightness value I_{GFP} .

Autofluorescence correction was applied to pool quantification by subtracting the red channel image from the green channel image multiplied by a correlation factor. By comparing wild type and GFP cell images we confirmed that when only the GFP exciting 488 nm wavelength laser was used the green channel image contained fluorescence intensity from GFP and autofluorescence, while the red channel contains only autofluorescence pixels, consistent with expectations from transmission spectra of known autofluorescent components in yeast cells. We measured the red channel autofluorescence pixels to be linearly proportional to the green channel autofluorescence pixels. The scaling factor between channels was determined by Slimfield imaging of the wild type yeast strain (i.e. non GFP) under the same conditions and comparing intensity values pixel-by-pixel in each channel. A linear relationship between pixels was found with scaling factor of 0.9 ± 0.1 .

Copy numbers of Mig1-GFP of the pool component were estimated using a previously developed CoPro algorithm (27). In brief, the cytoplasmic and nuclear pools were modelled as uniform fluorescence over spherical cells and nuclei using experimentally measured radii. A model PSF was integrated over these two volumes to create model nuclear and cytoplasmic images and then their relative contributions to the camera background and autofluorescence corrected GFP intensity image determined by solving a set of linear equations for each pixel. Dividing the contributions by the characteristic single GFP molecule intensity and correcting for out-of-plane foci yields the pool concentration.

Stoichiometry distributions were rendered as objective kernel density estimations (22) using a Gaussian kernel with bandwidth optimized for normally distributed data using standard MATLAB routines.

Stochastic optical reconstruction microscopy (STORM)

To photoswitch Mig1-mEos2, a 405 nm wavelength laser (Coherent Obis), attenuated to $\sim 1\text{mW}/\text{cm}^2$ was used in conjunction with the 488 nm and 561 nm lasers on the Slimfield microscope, similar to previous super-resolution imaging of yeast cells (79). The 405 nm laser light causes mEos2 to photoswitch from a green (excitable via the 488 nm laser) to a red

(excitable by the 561 nm laser) fluorescent state. Using low intensity 405 nm light generates photoactive fluorophore foci, photobleached by the 561 nm laser at a rate which results in an approximately steady-state concentration density in each live cell studied. The bright foci were tracked using the same parameters and criteria for spot acceptance as the Slimfield data. The tracks were then used to generate a super-resolved image heat map with 20nm pixel size by the summation of 2D Gaussian functions at each sub-pixel. Here, we assumed a sigma width of the 2D Gaussian function of 40nm to match the measured lateral precision following automated particle tracking of Mig1-mEos2 foci (27).

Fluorescent protein brightness characterization

We used a surface-immobilization assay described previously (21, 27) employing antibody conjugation to immobilize single molecules of GFP respectively onto the surface of plasma-cleaned BK7 glass microscope coverslips and imaged using the same buffer medium and imaging conditions as for live cell Slimfield experiments, resulting in integrated single-molecule peak intensity values for mGFP of $4,600 \pm 3,000$ (\pm half width half maximum, HWHM) counts. Similar experiments on unmodified purified Clontech eGFP generated peak intensity values of $4,700 \pm 2,000$ counts, statistically identical to that of mGFP (Student *t*-test, $p=0.62$) with no significant indication of multimerization effects from the measured distribution of foci intensity values. Similarly, Slimfield imaging and foci stoichiometry analysis on Mig1-mGFP and Mig1-eGFP cell strains were compared *in vivo* under high and low glucose conditions in two separate cell strains, resulting in distributions which were statistically identical (Pearson's χ^2 test comparing KDEs, Figure. 1 - Figure Supplement 2E and F). These results indicated no measurable differences between multimerization state or single-molecule foci intensity between mGFP and eGFP which enabled direct comparison between Mig1-eGFP cell strain data obtained from preliminary experiments here and from previous studies (16).

Maturation effects of mCherry and GFP were investigated by adding mRNA translation inhibitor antibiotic cycloheximide, final concentration 100 μ g/ml, for 1h (80), photobleaching cells, then monitoring any recovery in fluorescence as a metric for newly matured fluorescent material in the cell. Cells were prepared for microscopy as before but using cycloheximide in all subsequent preparation and imaging media and imaged using a commercial mercury-arc excitation fluorescence microscope Zeiss Axiovert 200M (Carl Zeiss MicroImaging) onto an ApoTome camera using a lower excitation intensity than for Slimfield imaging but a larger field of view, enabling a greater number of cells to be imaged simultaneously.

Surface-immobilized cells using strain YSH2863 were photobleached by continuous illumination for between 3min 40s to 4min until dark using separate filter sets 38HE and 43HE for GFP and mCherry excitation, respectively. Fluorescence images were acquired at subsequent time intervals up to 120min and analyzed using AxioVision software (Figure. S6). The background-corrected total cellular fluorescence intensity was quantified at each time point for each cell using ImageJ software. Comparison between Mig1-GFP fluorescence signal and the green channel signal from the parental strain BY4741, and the Nrd1-mCherry signal and the red channel signal from the parental strain, indicate fluorescence recovery after correction above the level of any autofluorescence contributions of <15% for GFP and mCherry over the timescale of our experiments, consistent with previous estimates of *in vivo* maturation times for GFP and mCherry (21, 22, 81).

Characterizing Mig1-GFP clusters *in vitro*

Using Slimfield microscopy under the same imaging conditions as for live cell microscopy we measured the fluorescent foci intensity of 1 μ g/ml solutions of purified Mig1-mGFP and mGFP using the normal imaging buffer of PBS, compared with the imaging buffer

supplemented with 1kDa molecular weight PEG at a concentration of 10% (w/v) used to reproduce cellular depletion forces (36, 75).

Circular dichroism measurements

Purified Mig1-mGFP was placed in 25 mM Na₂HPO₄, pH 7.0, by buffer exchange procedure with a Pur-A-Lyser Maxi dialysis Kit (Sigma Aldrich) for 3h at 4⁰C with constant stirring in 500 ml buffer. Circular dichroism measurements were performed on a Jasco J810 circular dichromator with Peltier temperature control and Biologic SFM300 stop-flow accessory on 0.16mg/ml Mig1-mGFP samples with or without 20% PEG-1000 at 20⁰C, from 260 to 200 nm, a 2 nm band width, 2 sec response time, at the speed of 100 nm/min. The resulting spectrum represents the average of 5 scans, indicating a typical SD error of ~0.1 mdeg ellipticity. Spectra from 25 mM Na₂HPO₄ and 25 mM Na₂HPO₄ with 20% (w/v) PEG were used as a background and subtracted from spectra of Mig1-mGFP without or with 20% (w/v) PEG respectively.

Immuno-gold electron microscopy

Cells for Mig1-GFP and Msn2-GFP strains as well as the wild type control strain containing no GFP were grown using the same conditions as for Slimfield imaging but pelleted down at the end of growth and prepared for immuno electron microscopy using an adaptation of the Tokuyasu cryosectioning method (82) following the same protocol that had been previously optimized for budding yeast cells (83) to generate ~90nm thick cryosections, with the exception that the sections were picked up on a drop of 2.3M sucrose, placed on the grid, then floated down on PBS, and then immunolabeled immediately, rather than storing on gelatine as occurred in the earlier protocol. The grids used were nickel, with a formvar/carbon support film. In brief, the immunolabeling protocol used a 0.05M glycine in PBS wash of each section for 5 min followed by a block of 10% goat serum in PBS (GS/PBS) pre-filtered through a 0.2 µm diameter filter. Then an incubation of 1 h with the primary antibody of rabbit polyclonal anti-GFP (ab6556, Abcam) at 1 in 250 dilution from stock in GS/PBS. Then five 3 min washes in GS/PBS. Then incubation for 45 min with the goat anti-IgG-rabbit secondary antibody labeled with 10nm diameter gold (EM.GAR10, BBI solutions) at a dilution of 1 in 10 from stock. Sections were then washed five more times in GS/PBS prior to chemical fixation in 1% glutaraldehyde in sodium phosphate buffer for 10 min, then washed in dH₂O five times for 3 min each and negative-stained using methyl cellulose 2% in 0.4% uranyl acetate, and then washed twice more in dH₂O prior to drying for 10 min. Drop sizes for staining, blocking and washing onto sections were 50 µl, while antibody incubations used 25 µl drops, all steps performed at room temperatures.

Electron microscopy was performed on these dried sections using a 120kV Tecnai 12 BioTWIN (FEI) electron microscope in transmission mode, and imaged onto an SIS Megaview III camera. From a total of ~150 control cells containing no GFP we could detect no obvious signs of gold labeling. Using approximately the same number of cells for each of the Mig1-GFP and Msn2-GFP strains all images showed evidence for at least one gold foci labeling in the cytoplasm, though labeling was largely absent from the nucleus possibly due to poor antibody accessibility into regions of tightly packed DNA since the combined Stokes radii from the primary and secondary antibodies is comparable to the mean effective DNA mesh size in the yeast nucleus of a few tens of nm (see Discussion section). We estimate that the thin cryosections occupy ~2.5% of the volume of an average yeast cell and so based on our copy number estimates from fluorescence microscopy in the accessible cytoplasmic compartment the maximum number of GFP available for labelling in each cryosection is ~20 molecules. We observed a range of 1-8 gold foci in total per cell across the GFP datasets and so the overall labelling efficiency in these experiments is low at typically 20% or less.

However, we observed 10 cells from a set of ~150 from each of the Mig-GFP and Msn2-GFP strains (i.e. ~7% of the total) which showed >1 gold foci clustering together inside an area of effective diameter ~50nm or less, with up to 7 gold foci per cluster being observed.

Bioinformatics analysis and structural modeling

Bioinformatics analysis was used to identify candidate promoter sequences in the budding yeast genome. The Mig1 target pattern sequence was identified based on 14 promoter sequences (37) using the IUPAC nucleotide code. The entire *S. cerevisiae* S288c genome was scanned in order to find all sequences that matched the pattern. The scanning was performed by RNABOB software (84), and collated for any further analysis and identification of the sequences lying within promoter regions. All information regarding *S. cerevisiae* genes was obtained from SGD database (<http://yeastgenome.org/>).

Using a consensus structural model for the budding yeast chromosome based on 3C data (38) we explored various different models of Mig1 binding to the putative promoter sequence identified from the bioinformatics analysis. We generated simulated images from these models adding experimentally realistic levels of signal and noise, and ran these data through the same foci detection and analysis software as for the real live cell data using identical parameters throughout. We then compared these results to the measured experimental stoichiometry (Figure. 4C). Monomer models assume that a single Mig1 molecule binds to a target promoter site, whereas cluster models assume that a cluster comprising 7 Mig1 molecules (based on our observations of stoichiometry periodicity) binds a single target promoter. Copy number analysis indicated 190 Mig1 molecules per cell on average associated with foci. In the monomer model (Fig. 4C) all 109 promoter sites were assigned a Mig1 molecule and the remaining 81 Mig1 molecules were placed randomly in the 222 remaining Mig1 target binding sites within the rest of the genome. In the DNA cluster model (Figure. 4 – Figure Supplement 1) we randomly assigned the observed 190 Mig1 molecules in foci into just 27 clusters to Mig1 target promoter sites. We also tested two nuclear envelope (NE) variants of both models, to account for the trans-nuclear tracks: here, typically ~7 Mig1 were observed translocating from the nucleus to the cytoplasm at *glucose* (+) within the microscope's depth of field; extrapolating this value over the whole nucleus this indicates ~130 Mig1 molecules within the nucleus but less than a single PSF width from the nuclear envelope prior to export to the cytoplasm. We simulated this effect using either 130 Mig1 molecules as Mig1 monomers or as 18 (i.e. ~130/7) 7-mer clusters at random 3D coordinates at the simulated nuclear envelope position in the 3C model. Finally, to generate the best fit Mig1 cluster model, we obtained an optimized fit to the data with a mixed population model with 75% of cells in the NE cluster model and 25% in the DNA cluster model. We note here that the monomer model can produce higher apparent stoichiometry due to the increased density of resulting foci (although the same density of Mig1).

We used bioinformatics to investigate the extent of intrinsic disorder in the amino acid sequence of budding yeast Mig1 and Msn2 proteins as well as the *E. coli lac* repressor LacI, employing the Predictor of Natural Disordered Regions (PONDR) algorithm (85) (online tool <http://www.pondr.com/cgi-bin/PONDR/pondr.cgi>) with a VL-XT algorithm. We also used the secondary structure prediction algorithm of PyMOL (<http://www.pymolwiki.org/index.php/Dss>) to highlight disordered and structured regions and display the unfolded protein chain, and used PSI-BLAST multiple sequence alignment to determine conserved structural features of Mig1 for the Zn finger motif in combination with the DISOPRED (62) algorithm as a comparison to PONDR, which produced very similar results (online tool <http://www.yeastrc.org/pdr/>).

Oligomerization state of Mig1-GFP in the ‘pool’

Experimental *in vitro* assays of surface immobilized GFP coupled to simulations trained on these single-molecule intensity measurements but using noise levels comparable to *in vivo* cellular imaging conditions (27) indicate single-molecule sensitivity of GFP detection under our millisecond imaging conditions. However, if the nearest neighbor separation of individual GFP ‘foci’ are less than the optical resolution limit w of our microscope (which we measure as ~230 nm for GFP imaging) then distinct fluorescent foci will not be detected and instead will be manifest as a diffusive ‘pool’.

If each GFP ‘foci’ in the pool has a mean stoichiometry S then the mean number of GFP foci, F , in the pool is n_{pool}/S and the ‘pool’ condition for nearest neighbor foci separation s indicates that $s < w$.

The estimated range of mean total pool copy number from nucleus and cytoplasm combined, n_{pool} , is ~590-1,100 molecules depending on extracellular glucose conditions. Approximating the cell volume as equal to the combined volumes of all uniformly separated foci in the pool (equal to the total number of foci multiplied by the volume of an equivalent sphere of radius r) indicates that $F \cdot 4\pi r^3/3 = 4\pi d^3/3$, thus $r = d/F^{1/3}$, where we use the mean measured cell diameter d of ~5 μm .

However, mobile foci with a microscopic diffusion coefficient D will diffuse a mean two-dimensional distance b in focal plane of $(4D\Delta t)^{1/2}$ in a camera sampling time window Δt of 5 ms. Using $D \sim 6 \mu\text{m}^2 \text{s}^{-1}$ as a lower limit based on the measured diffusion of low stoichiometry cytoplasmic Mig1-GFP foci detected indicates $b \sim 340$ nm so the movement-corrected estimate for s is $r-b$, thus $s < w$ indicates that $r < b+w$, or $d/F^{1/3} < b+w$.

Therefore, $d(S/n_{pool})^{1/3} < b+w$, and $S < n_{pool}((b+w)/d)^3$. Using ~590-1,100 molecules from the measured mean range of n_{pool} indicates that the upper limit for S is in the range 0.8-1.4; in other words, Mig1-GFP foci in the pool are consistent with being a monomer.

Analysis of the mobility of foci

For each accepted foci track the mean square displacement (MSD) was calculated from the optimized intensity centroid at time t of $(x(t), y(t))$ assuming a tracks of N consecutive image frames at a time interval $\tau = n\Delta t$ is (86, 87) where n is a positive integer is:

$$MSD(\tau) = MSD(n\Delta t) = \frac{1}{N-1-n} \sum_{i=1}^{N-1-n} \{ [x(i\Delta t + n\Delta t) - x(i\Delta t)]^2 + [y(i\Delta t + n\Delta t) - y(i\Delta t)]^2 \}$$

$$= 4D\tau + 4\sigma^2$$

Here σ is the lateral (xy) localization precision which we estimate as ~40 nm (27). The microscopic diffusion coefficient D was then estimated from the gradient of a linear fit to the first four time interval data points of the MSD vs τ relation for each accepted foci track.

To determine the proportion of mobile and immobile Mig1-GFP fluorescent foci we adapted an approach based on cumulative probability-distance distribution analysis (12). Here we generated cumulative distribution functions (CDFs) for all nuclear and cytoplasmic tracks, such that the CDF in each dataset is the probability distribution function p_c associated with r^2 , the square of the displacement between the first and second data points in each single track, which was generated for each track by calculating the proportion of all tracks in a dataset which have a value of r^2 less than that measured for that one track. The simplest CDF model assumes a Brownian diffusion propagator function $f(r^2)$ for a single effective diffusion coefficient component of:

$$f(r^2) = \frac{1}{4\pi D\Delta t} \exp\left(-\frac{r^2}{4D\Delta t}\right)$$

Here, D is the effective diffusion coefficient and Δt is image sampling time per frame (i.e. in our case 5 ms). This gives a CDF single component solution of the form:

$$p_c(r^2) = 1 - \exp\left(-\frac{r^2}{4D\Delta t}\right)$$

We investigated both single and more complex multi-component CDF models using either 1, 2 or 3 different D values in a weighted sum model of:

$$p_c(r^2) = \sum_{i=1}^n A_i \left(1 - \exp\left(-\frac{r^2}{4D_i\Delta t}\right)\right)$$

Here n is 1, 2 or 3. Multi-component fits were only chosen if they lowered the reduced χ^2 by >10%. For cytoplasmic foci at *glucose* (+/-) and for nuclear foci at *glucose* (-) this indicated single component fits for diffusion coefficient with a D of $\sim 1-2 \mu\text{m}^2/\text{s}$, whereas nuclear foci at *glucose* (+) were fitted using two components of D , $\sim 20\%$ with a relatively immobile component, $D \sim 0.1-0.2 \mu\text{m}^2/\text{s}$, and the remainder a relatively mobile component, $D \sim 1-2 \mu\text{m}^2/\text{s}$, while using three components produced no statistically significant improvement to the fits. These values of D agreed to within experimental error to those obtained using a different method which fitted two analytical Gamma functions to the distribution of all calculated microscopic diffusion coefficients of tracked foci in the nucleus at *glucose* (+), which assumed a total probability distribution function p_γ of the form: (29)

$$p_\gamma(x, D) = \sum_{i=1}^2 \frac{A_i (m/D)^m x^{n-1} \exp(-mx/D)}{(m-1)!}$$

Here, m is the number of steps in the MSD vs τ trace for each foci track used to calculate D (i.e. in our instance $m=4$).

We also probed longer time scale effects on foci mobility for each accepted foci trajectory. Here, average MSD values were generated by calculating mean MSD values for corresponding time interval values across all foci trajectories in each dataset, but pooling traces into low stoichiometry (≤ 20 Mig1-GFP molecules per foci) and high stoichiometry (> 20 Mig1-GFP molecules per foci). We compared different diffusion models over a 30 ms time interval scale, corresponding to the shortest time interval range from any of the mean MSD trace datasets.

We found in all cases that mean MSD traces could be fitted well (χ^2 values in the range 1-12) using a subdiffusion model of precision-corrected MSD = $4\sigma^2 + 4K\tau^\alpha$, where α the anomalous diffusion parameter and K is the transport parameter, analogous to the diffusion coefficient D in pure Brownian diffusion. Optimized fits indicated values of K in the range $0.08-0.2 \mu\text{m}^2/\text{s}$ and those for α of $\sim 0.4-0.8$. Corresponding fits to a purely Brownian diffusion model (i.e. $\alpha = 1$) generated much poorer fits (χ^2 values in the range 4-90).

We used both short timescale CDF analysis and longer timescale MSD analysis of Mig1 tracks to try to gain as complete a picture of Mig1 mobility as possible. Short timescales

avoid bias from photobleaching and diffusion out of the focal plane but longer timescales sample more of the cellular environment.

Analyzing trans-nuclear tracks

The segmentation boundary output for the nucleus was fitted with a smoothing spline function, with smoothing parameter $p = 0.9992$ to sub-pixel precision. Trajectories which contained points on either side of the nuclear boundary were considered trans-nuclear. The crossing point on the nuclear boundary was found by linearly interpolating between the first pair of points either side of the nuclear boundary. Coordinates were normalized to this point and the crossing time and were rotated such that y' and x' lie perpendicular and parallel to the membrane crossing point.

Investigating Mig1-GFP molecular turnover

Turnover of Mig1-GFP was investigated using fluorescence recovery after photobleaching (FRAP). In brief a 200 ms 10mW focused laser beam pulse of lateral width $\sim 1 \mu\text{m}$ was used to photobleach the fluorescently-labelled nuclear contents on a cell-by-cell basis and then ≤ 10 Slimfield images were recorded over different timescales spanning a range from 100 ms to $\sim 1,000$ s. The copy number of pool and foci in each image at subsequent time points t post focused laser bleach was determined as described and corrected for photobleaching. These post-bleach photoactive Mig1-GFP copy number values $C(t)$ could then be fitted using a single exponential recovery function:

$$C(t) = C(0)(1 - \exp(-t/t_R))$$

Where t_R is the characteristic recovery (i.e. turnover) time (20). These indicated a value of 133 ± 20 s (\pm SEM) for nuclear foci at glucose (+), and 3 ± 14 s for nuclear pool at glucose (+) and (-).

Modeling the effective diameter of clusters

The effective diameter d of a cluster was estimated from the measured point spread function width pf_{foci} (defined at twice sigma value of the equivalent Gaussian fit from our single particle tracking algorithm) corrected for the blur due to particle diffusion in the camera exposure time of Δt as:

$$d = p_{foci} - p_{GFP} - \sqrt{4D\Delta t}$$

Where D is the measured microscopic diffusion coefficient for that track and p_{GFP} is the measured point spread function width of surface-immobilized GFP (i.e. twice the sigma width of 230nm measured in our microscope, or 460nm). We explored a heuristic packing model of $d \sim S^a$ for Mig1-GFP monomers in each cluster, such that a tightly packed spherical cluster of volume V composed of S smaller ca. spherical monomers each of volume V_I and diameter d_I varied as $V = S.V_I$ thus $4\pi(d/2)^3 = S.4\pi(d_I/2)^3$, thus in the specific instance of a perfect spherical cluster model $a = 1/3$.

In principle, for general shapes of clusters for different packing conformations we expect $0 \leq a \leq 1$ such that e.g. if clusters pack as a long, thin rod of Mig1 monomers which rotates isotropically during time Δt , then $a = 1$. Whereas, if Mig1 monomers bind to a putative additional 'anchor' type structure to occupy available binding sites in forming a cluster, such that the size of the cluster does not significantly change with S but is dependent

on the size of the putative anchor structure itself, then $a = 0$. Our optimized fits indicate $a = 0.32 \pm 0.06$ (\pm SEM), i.e. consistent with an approximate spherical shape cluster model.

Modeling the probability of overlap in *in vitro* fluorescent protein characterization

The probability that two or more fluorescent protein foci are within the diffraction limit of our microscope in the *in vitro* characterization assays was determined using a previously reported Poisson model (26) to be ~10% at the *in vitro* protein concentrations used here. Such overlapping fluorescent proteins are detected as higher apparent stoichiometry foci.

PP7 RNA labelling and overlap integral

Similar Slimfield microfluidics experiments were performed on Mig1-mCherry and Mig1-mCherry Δ Znf strains containing 24 transcriptional reporter PP7 markers on the GYS1 gene and transformed with plasmids for the PP7 protein labelled with 2 GFPs. Mig1 foci are present at *glucose* (+) and upon switching to *glucose* (-) PP7 foci appear in similar locations to the Mig1 foci. Although Mig1 foci are mobile, the microscopic diffusion coefficient D for immobilized Mig1 is a putative overestimate for the equivalent D of the underlying target gene loci, $0.15 \mu\text{m}^2/\text{s}$ from CDF. The plateau of the MSD vs tau plot in Figure. 3B gives an estimate of the gene loci mobility range in space (although still an overestimate) and is $\sim 0.05 \mu\text{m}^2$. The square root of this is less than PSF width, and so colocalization between Mig1 and PP7 foci is expected.

The extent of colocalization between Mig1-mCherry and PP7-GFP detected foci was determined by calculating the overlap integral between each pair, whose centroids were within 5 pixels of each other. Assuming two normalized, 2D Gaussian intensity distributions g_1 and g_2 , for green and red foci respectively, centered around (x_1, y_1) with sigma width σ_1 , and around (x_2, y_2) with width σ_2 , the overlap integral v is analytically determined as:

$$v = \exp\left(-\frac{\Delta r^2}{2(\sigma_1^2 + \sigma_2^2)}\right)$$

Where

$$\Delta r^2 = (x_1^2 - x_2^2)^2 + (y_1^2 - y_2^2)^2$$

Previous studies have used an overlap integral of over 0.75 as a criteria for colocalization (26).

Software and DNA sequence access

All our bespoke software developed, and Mig1 secondary structure prediction 3D coordinates *pymolMig1.pdb*, are freely and openly accessible via <https://sourceforge.net/projects/york-biophysics/>. The bespoke plasmid sequence information for the GFP reporter is openly accessible via <https://www.addgene.org/75360/>.

Statistical tests and replicates

All statistical tests used are two-sided unless stated otherwise. For Slimfield imaging each cell can be defined as a biological replicate sampled from the cell population. We chose sample sizes of at least 30 cells which generated reasonable estimates for the sampled stoichiometry distributions, similar to those of previous *in vivo* Slimfield studies (20).

Technical replicates are not possible with the irreversible photobleaching assay, however, the

noise in all light microscopy experiments has been independently characterized for the imaging system used previously (27).

Acknowledgments

Supported by the Biological Physical Sciences Institute, Royal Society, MRC (grant MR/K01580X/1), BBSRC (grant BB/N006453/1), Swedish Research Council and European Commission via Marie Curie-Network for Initial training ISOLATE (Grant agreement nr: 289995) and the Marie Curie Alumni Association. We thank Magnus Alm Rosenblad and Sarah Shammass for assistance with RNABOB and PONDR, Marija Cvijovic and Michael Law for help with qPCR data analysis, Andrew Leech and Meg Stark for help with CD and EM. Thanks to Mark Johnston (CU Denver) for donation of Mig1 phosphorylation mutant plasmid, and Michael Elowitz (Caltech) for donation of the Mig1/Msn2/PP7 and Zn finger deletion strain.

Conflict of interest

All the authors declare that they have no conflict of interests.

References

1. F. Jacob, J. Monod, Genetic regulatory mechanisms in the synthesis of proteins. *J. Mol. Biol.* **3**, 318–356 (1961).
2. J. Gertz, E. D. Siggia, B. A. Cohen, Analysis of combinatorial cis-regulation in synthetic and genomic promoters. *Nature*. **457**, 215–8 (2009).
3. O. G. Berg, R. B. Winter, P. H. Von Hippel, Diffusion-driven mechanisms of protein translocation on nucleic acids. 1. Models and theory. *Biochemistry*. **20**, 6929–6948 (1981).
4. A. Mahmutovic, O. G. Berg, J. Elf, What matters for lac repressor search in vivo--sliding, hopping, intersegment transfer, crowding on DNA or recognition? *Nucleic Acids Res.* **43**, 3454–64 (2015).
5. S. E. Halford, J. F. Marko, How do site-specific DNA-binding proteins find their targets? *Nucleic Acids Res.* **32**, 3040–52 (2004).
6. D. M. Gowers, S. E. Halford, Protein motion from non-specific to specific DNA by three-dimensional routes aided by supercoiling. *EMBO J.* **22**, 1410–8 (2003).
7. S. T. Whiteside, S. Goodbourn, Signal transduction and nuclear targeting: regulation of transcription factor activity by subcellular localisation. *J. Cell Sci.* **104** (Pt 4, 949–55 (1993).
8. C. T. Harbison *et al.*, Transcriptional regulatory code of a eukaryotic genome. *Nature*. **431**, 99–104 (2004).
9. H. G. Schmidt, S. Sewitz, S. S. Andrews, K. Lipkow, An Integrated Model of Transcription Factor Diffusion Shows the Importance of Intersegmental Transfer and Quaternary Protein Structure for Target Site Finding. **9** (2014), doi:10.1371/journal.pone.0108575.
10. G.-W. Li, X. S. Xie, Central dogma at the single-molecule level in living cells. *Nature*. **475**, 308–15 (2011).
11. P. Hammar *et al.*, The lac repressor displays facilitated diffusion in living cells. *Science*. **336**, 1595–8 (2012).
12. J. C. M. Gebhardt *et al.*, Single-molecule imaging of transcription factor binding to DNA in live mammalian cells. *Nat. Methods*. **10**, 421–6 (2013).
13. J. O. Nehlin, M. Carlberg, H. Ronne, Control of yeast GAL genes by MIG1 repressor: a transcriptional cascade in the glucose response. *EMBO J.* **10**, 3373–7 (1991).
14. E. Frolova, Binding of the glucose-dependent Mig1p repressor to the GAL1 and GAL4 promoters in vivo: regulation by glucose and chromatin structure. *Nucleic Acids Res.* **27**, 1350–1358 (1999).
15. M. J. De Vit, J. a Waddle, M. Johnston, Regulated nuclear translocation of the Mig1 glucose repressor. *Mol. Biol. Cell.* **8**, 1603–18 (1997).
16. L. Bendrioua *et al.*, Yeast AMP-activated Protein Kinase Monitors Glucose Concentration Changes and Absolute Glucose Levels. *J. Biol. Chem.* **289**, 12863–75 (2014).
17. S. Shashkova, A. J. M. Wollman, M. C. Leake, S. Hohmann, The yeast Mig1 transcriptional repressor is dephosphorylated by glucose-dependent and -independent mechanisms. *FEMS Microbiol. Lett.* **364** (2017), doi:10.1093/femsle/fnx133.

- 1245 18. Y. Lin, C. H. Sohn, C. K. Dalal, L. Cai, M. B. Elowitz, Combinatorial gene regulation
1246 by modulation of relative pulse timing. *Nature*. **527**, 54–58 (2015).
- 1247 19. M. Plank, G. H. Wadhams, M. C. Leake, Millisecond timescale slimfield imaging and
1248 automated quantification of single fluorescent protein molecules for use in probing
1249 complex biological processes. *Integr. Biol. (Camb)*. **1**, 602–12 (2009).
- 1250 20. R. Reyes-Lamothe, D. J. Sherratt, M. C. Leake, Stoichiometry and architecture of
1251 active DNA replication machinery in *Escherichia coli*. *Science*. **328**, 498–501 (2010).
- 1252 21. A. Badrinarayanan, R. Reyes-Lamothe, S. Uphoff, M. C. Leake, D. J. Sherratt, In vivo
1253 architecture and action of bacterial structural maintenance of chromosome proteins.
1254 *Science*. **338**, 528–31 (2012).
- 1255 22. M. C. Leake *et al.*, Stoichiometry and turnover in single, functioning membrane
1256 protein complexes. *Nature*. **443**, 355–8 (2006).
- 1257 23. D. A. Zacharias, J. D. Violin, A. C. Newton, R. Y. Tsien, Partitioning of lipid-
1258 modified monomeric GFPs into membrane microdomains of live cells. *Science*. **296**,
1259 913–6 (2002).
- 1260 24. S. A. McKinney, C. S. Murphy, K. L. Hazelwood, M. W. Davidson, L. L. Looger, A
1261 bright and photostable photoconvertible fluorescent protein. *Nat. Methods*. **6**, 131–3
1262 (2009).
- 1263 25. H. Miller, Z. Zhou, A. J. M. Wollman, M. C. Leake, Superresolution imaging of single
1264 DNA molecules using stochastic photoblinking of minor groove and intercalating
1265 dyes. *Methods*. **88**, 81–8 (2015).
- 1266 26. I. Llorente-Garcia *et al.*, Single-molecule in vivo imaging of bacterial respiratory
1267 complexes indicates delocalized oxidative phosphorylation. *Biochim. Biophys. Acta*.
1268 **1837**, 811–824 (2014).
- 1269 27. A. J. M. Wollman, M. C. Leake, Millisecond single-molecule localization microscopy
1270 combined with convolution analysis and automated image segmentation to determine
1271 protein concentrations in complexly structured, functional cells, one cell at a time.
1272 *Faraday Discuss.* **184**, 401–24 (2015).
- 1273 28. M. J. DeVit, M. Johnston, The nuclear exportin Msn5 is required for nuclear export of
1274 the Mig1 glucose repressor of *Saccharomyces cerevisiae*. *Curr. Biol.* **9**, 1231–1241
1275 (1999).
- 1276 29. M. Stracy *et al.*, Live-cell superresolution microscopy reveals the organization of RNA
1277 polymerase in the bacterial nucleoid. *Proc. Natl. Acad. Sci. U. S. A.* **112**, E4390-9
1278 (2015).
- 1279 30. I. Izeddin *et al.*, Single-molecule tracking in live cells reveals distinct target-search
1280 strategies of transcription factors in the nucleus. *Elife*. **3** (2014),
1281 doi:10.7554/eLife.02230.
- 1282 31. S. A. Adam, The nuclear pore complex. *Genome Biol.* **2** (2001) REVIEWS007.
- 1283 32. C. Strambio-De-Castillia, M. Niepel, M. P. Rout, The nuclear pore complex: bridging
1284 nuclear transport and gene regulation. *Nat. Rev. Mol. Cell Biol.* **11**, 490–501 (2010).
- 1285 33. W. Yang, J. Gelles, S. M. Musser, Imaging of single-molecule translocation through
1286 nuclear pore complexes. *Proc. Natl. Acad. Sci. U. S. A.* **101**, 12887–12892 (2004).
- 1287 34. A. R. Lowe *et al.*, Selectivity mechanism of the nuclear pore complex characterized by

single cargo tracking. *Nature*. **467**, 600–603 (2010).

35. M. A. Treitel, M. Carlson, Repression by SSN6-TUP1 is directed by MIG1, a repressor/activator protein. *Proc. Natl. Acad. Sci. U. S. A.* **92**, 3132–6 (1995).

36. Y. Phillip, G. Schreiber, Formation of protein complexes in crowded environments--from in vitro to in vivo. *FEBS Lett.* **587**, 1046–52 (2013).

37. M. Lundin, J. O. Nehlin, H. Ronne, Importance of a flanking AT-rich region in target site recognition by the GC box-binding zinc finger protein MIG1. *Mol. Cell. Biol.* **14**, 1979–1985 (1994).

38. Z. Duan *et al.*, A three-dimensional model of the yeast genome. *Nature*. **465**, 363–7 (2010).

39. I. Unnikrishnan, S. Miller, M. Meinke, D. C. LaPorte, Multiple positive and negative elements involved in the regulation of expression of GSY1 in *Saccharomyces cerevisiae*. *J. Biol. Chem.* **278**, 26450–7 (2003).

40. V. N. Uversky, I. M. Kuznetsova, K. K. Turoverov, B. Zaslavsky, Intrinsically disordered proteins as crucial constituents of cellular aqueous two phase systems and coacervates. *FEBS Lett.* **589**, 15–22 (2015).

41. J. A. Toretsky, P. E. Wright, Assemblages: functional units formed by cellular phase separation. *J. Cell Biol.* **206**, 579–88 (2014).

42. D. S. Goodsell, A. J. Olson, Structural Symmetry and Protein Function. *Annu. Rev. Biophys. Biomol. Struct.* **29**, 105–153 (2000).

43. J. H. Fong *et al.*, Intrinsic Disorder in Protein Interactions: Insights From a Comprehensive Structural Analysis. *PLoS Comput. Biol.* **5**, e1000316 (2009).

44. K. Sode, S. Ochiai, N. Kobayashi, E. Usuzaka, Effect of reparation of repeat sequences in the human alpha-synuclein on fibrillation ability. *Int. J. Biol. Sci.* **3**, 1–7 (2007).

45. C. Avitabile *et al.*, Circular Dichroism studies on the interactions of antimicrobial peptides with bacterial cells. *Sci. Rep.* **4**, 337–360 (2014).

46. H. Nishi, J. H. Fong, C. Chang, S. A. Teichmann, A. R. Panchenko, Regulation of protein-protein binding by coupling between phosphorylation and intrinsic disorder: analysis of human protein complexes. *Mol. Biosyst.* **9**, 1620–6 (2013).

47. D. Mazza, A. Abernathy, N. Golob, T. Morisaki, J. G. McNally, A benchmark for chromatin binding measurements in live cells. *Nucleic Acids Res.* **40**, e119–e119 (2012).

48. D. Normanno *et al.*, Probing the target search of DNA-binding proteins in mammalian cells using TetR as model searcher. *Nat. Commun.* **6**, 7357 (2015).

49. P. G. Needham, R. J. Trumbly, In vitro characterization of the Mig1 repressor from *Saccharomyces cerevisiae* reveals evidence for monomeric and higher molecular weight forms. *Yeast*. **23**, 1151–66 (2006).

50. I. I. Cisse *et al.*, Real-Time Dynamics of RNA Polymerase II Clustering in Live Human Cells. *Science (80-.)*. **341**, 664–667 (2013).

51. W.-K. Cho *et al.*, RNA Polymerase II cluster dynamics predict mRNA output in living cells. *Elife*. **5** (2016), doi:10.7554/eLife.13617.

52. J. Qian *et al.*, B Cell Super-Enhancers and Regulatory Clusters Recruit AID

- 1330 Tumorigenic Activity. *Cell*. **159**, 1524–1537 (2014).
- 1331 53. M. Mir *et al.*, Dense Bicoid Hubs Accentuate Binding along the Morphogen Gradient.
1332 *bioRxiv* (2017).
- 1333 54. T. S. Karpova *et al.*, Concurrent fast and slow cycling of a transcriptional activator at
1334 an endogenous promoter. *Science*. **319**, 466–9 (2008).
- 1335 55. R. Rohs *et al.*, Origins of specificity in protein-DNA recognition. *Annu. Rev. Biochem.*
1336 **79**, 233–69 (2010).
- 1337 56. J. Elf, G.-W. Li, X. S. Xie, Probing Transcription Factor Dynamics at the Single-
1338 Molecule Level in a Living Cell. *Science* (80-.). **316**, 1191–1194 (2007).
- 1339 57. M. A. Lomholt, B. van den Broek, S.-M. J. Kalisch, G. J. L. Wuite, R. Metzler,
1340 Facilitated diffusion with DNA coiling. *Proc. Natl. Acad. Sci. U. S. A.* **106**, 8204–8
1341 (2009).
- 1342 58. B. van den Broek, M. A. Lomholt, S.-M. J. Kalisch, R. Metzler, G. J. L. Wuite, How
1343 DNA coiling enhances target localization by proteins. *Proc. Natl. Acad. Sci. U. S. A.*
1344 **105**, 15738–42 (2008).
- 1345 59. A. Esadze, J. Iwahara, Stopped-Flow Fluorescence Kinetic Study of Protein Sliding
1346 and Intersegment Transfer in the Target DNA Search Process. *J. Mol. Biol.* **426**, 230–
1347 244 (2014).
- 1348 60. D. M. Gowers, G. G. Wilson, S. E. Halford, Measurement of the contributions of 1D
1349 and 3D pathways to the translocation of a protein along DNA. *Proc. Natl. Acad. Sci.*
1350 *U. S. A.* **102**, 15883–8 (2005).
- 1351 61. B. Xue, A. K. Dunker, V. N. Uversky, Orderly order in protein intrinsic disorder
1352 distribution: disorder in 3500 proteomes from viruses and the three domains of life. *J.*
1353 *Biomol. Struct. Dyn.* **30**, 137–49 (2012).
- 1354 62. J. J. Ward, J. S. Sodhi, L. J. McGuffin, B. F. Buxton, D. T. Jones, Prediction and
1355 functional analysis of native disorder in proteins from the three kingdoms of life. *J.*
1356 *Mol. Biol.* **337**, 635–45 (2004).
- 1357 63. G. Rivas, J. A. Fernández, A. P. Minton, Direct observation of the enhancement of
1358 noncooperative protein self-assembly by macromolecular crowding: indefinite linear
1359 self-association of bacterial cell division protein FtsZ. *Proc. Natl. Acad. Sci. U. S. A.*
1360 **98**, 3150–5 (2001).
- 1361 64. R. Babazadeh *et al.*, Osmostress-induced cell volume loss delays yeast Hog1 signaling
1362 by limiting diffusion processes and by Hog1-specific effects. *PLoS One*. **8**, e80901
1363 (2013).
- 1364 65. A. Miermont *et al.*, Severe osmotic compression triggers a slowdown of intracellular
1365 signaling, which can be explained by molecular crowding. *Proc. Natl. Acad. Sci. U. S.*
1366 *A.* **110**, 5725–30 (2013).
- 1367 66. J. Ma, W. Yang, Three-dimensional distribution of transient interactions in the nuclear
1368 pore complex obtained from single-molecule snapshots. *Proc. Natl. Acad. Sci. U. S. A.*
1369 **107**, 7305–7310 (2010).
- 1370 67. I. Axelsson, Characterization of proteins and other macromolecules by agarose gel
1371 chromatography. *J. Chromatogr. A.* **152**, 21–32 (1978).
- 1372 68. M. A. Hink *et al.*, Structural dynamics of green fluorescent protein alone and fused

- with a single chain Fv protein. *J. Biol. Chem.* **275**, 17556–60 (2000).
69. L.-F. Liang, X. Da, T.-S. Chen, Y.-H. Pei, [Nucleoplasmic viscosity of living cells investigated by fluorescence correlation spectroscopy]. *Guang Pu Xue Yu Guang Pu Fen Xi.* **29**, 459–62 (2009).
70. H.-J. Schüller, Transcriptional control of nonfermentative metabolism in the yeast *Saccharomyces cerevisiae*. *Curr. Genet.* **43**, 139–60 (2003).
71. J. Liu *et al.*, Intrinsic disorder in transcription factors. *Biochemistry.* **45**, 6873–88 (2006).
72. V. N. Uversky, V. B. Patel, Intrinsically disordered proteins and their (disordered) proteomes in neurodegenerative disorders (2015), doi:10.3389/fnagi.2015.00018.
73. E. M. Rubenstein *et al.*, Access denied: Snf1 activation loop phosphorylation is controlled by availability of the phosphorylated threonine 210 to the PP1 phosphatase. *J. Biol. Chem.* **283**, 222–30 (2008).
74. R. D. Gietz, R. H. Schiestl, Frozen competent yeast cells that can be transformed with high efficiency using the LiAc/SS carrier DNA/PEG method. *Nat. Protoc.* **2**, 1–4 (2007).
75. J. Warringer *et al.*, Trait variation in yeast is defined by population history. *PLoS Genet.* **7**, e1002111 (2011).
76. C. Geijer *et al.*, Initiation of the transcriptional response to hyperosmotic shock correlates with the potential for volume recovery. *FEBS J.* **280**, 3854–67 (2013).
77. S. Shashkova, M. C. Leake, Single-molecule fluorescence microscopy review: shedding new light on old problems. *Biosci. Rep.* **37** (2017).
78. A.-K. Gustavsson *et al.*, Sustained glycolytic oscillations in individual isolated yeast cells. *FEBS J.* **279**, 2837–47 (2012).
79. E. M. Puchner, J. M. Walter, R. Kasper, B. Huang, W. A. Lim, Counting molecules in single organelles with superresolution microscopy allows tracking of the endosome maturation trajectory, doi:10.1073/pnas.1309676110.
80. L. H. Hartwell, J. Culotti, B. Reid, Genetic control of the cell-division cycle in yeast. I. Detection of mutants. *Proc. Natl. Acad. Sci. U. S. A.* **66**, 352–9 (1970).
81. A. Khmelinskii *et al.*, Tandem fluorescent protein timers for in vivo analysis of protein dynamics. *Nat. Biotechnol.* **30**, 708–14 (2012).
82. K. T. Tokuyasu, A technique for ultracryotomy of cell suspensions and tissues. *J. Cell Biol.* **57**, 551–65 (1973).
83. J. Griffith, M. Mari, A. De Mazière, F. Reggiori, A Cryosectioning Procedure for the Ultrastructural Analysis and the Immunogold Labelling of Yeast *Saccharomyces cerevisiae*. *Traffic.* **9**, 1060–1072 (2008).
84. N. J. Riccitelli, A. Lupták, Computational discovery of folded RNA domains in genomes and in vitro selected libraries. *Methods.* **52**, 133–40 (2010).
85. Z. Obradovic, K. Peng, S. Vucetic, P. Radivojac, A. K. Dunker, Exploiting heterogeneous sequence properties improves prediction of protein disorder. *Proteins.* **61 Suppl 7**, 176–82 (2005).
86. D. Gross, W. Webb, in *Spectroscopic Membrane Probes*, L. Loew, Ed. (CRC Press,

1415 ed. 2, 1988), pp. 19–45.

1416 87. X. Michalet, Mean square displacement analysis of single-particle trajectories with
 1417 localization error: Brownian motion in an isotropic medium. *Phys. Rev. E*. **82**, 41914
 1418 (2010).

1419 88. M. C. Leake, D. Wilson, M. Gautel, R. M. Simmons, The elasticity of single titin
 1420 molecules using a two-bead optical tweezers assay. *Biophys. J.* **87**, 1112–35 (2004).

1421 89. M. C. Leake, D. Wilson, B. Bullard, R. M. Simmons, M. R. Bubb, The elasticity of
 1422 single kettin molecules using a two-bead laser-tweezers assay. *FEBS Lett.* **535** (2003),
 1423 doi:10.1016/S0014-5793(02)03857-7.

1424 90. P. Rice, I. Longden, A. Bleasby, EMBOSS: the European Molecular Biology Open
 1425 Software Suite. *Trends Genet.* **16**, 276–7 (2000).

1426 91. M. C. Schmidt, R. R. McCartney, beta-subunits of Snf1 kinase are required for kinase
 1427 function and substrate definition. *EMBO J.* **19**, 4936–43 (2000).

1428 92. G. Berben, J. Dumont, V. Gilliquet, P. A. Bolle, F. Hilger, The YDp plasmids: a
 1429 uniform set of vectors bearing versatile gene disruption cassettes for *Saccharomyces*
 1430 *cerevisiae*. *Yeast*. **7**, 475–7 (1991).

1431

Legends

Table 1. *S. cerevisiae* cell strains and plasmids. List of all strains and plasmids used in this study.

Table 2. Copy number data. Mean average and SD of copy number in pool and foci in each compartment.

Table 3. Foci tracking data. Mean average, SD and mean number detected per cell (N) of stoichiometry values (molecules), and microscopic diffusion coefficients D in each compartment detected within the depth of field.

Table 4. *snf1Δ* foci tracking and copy number data. Upper panel: Mean average, SD and mean number detected per cell (N) of stoichiometry values (molecules), and microscopic diffusion coefficients D in each compartment detected within the depth of field. Lower panel: Mean average and SD of copy number in pool and foci in each compartment.

Table 5. Number of potential Mig1 target promoter sites per chromosome. List of *S. cerevisiae* chromosomes indicating the length of a chromosome, total number of potential Mig1 target sites identified and then the number of sites on promoters assuming a promoter region up to 500bp upstream of a gene.

Table 6. Bioinformatics analysis for intrinsically disordered sequences. Predictions for the presence of intrinsically disordered sequences in Mig1, Msn2 and LacI, and of the positions of phosphorylation sites in Mig1 and Msn2.

Video 1. Dual-color fluorescence microscopy assay at *glucose* (+). Example cell showing *glucose* (+) nuclear Mig1-GFP localization (green, distinct foci black arrows), Nrd1-mCherry (red) and segmented cell body (orange) and nuclear envelope (cyan) indicated, slowed 15x.

Video 2. Dual-color fluorescence microscopy assay at *glucose* (-). Example cell showing *glucose* (-) Mig1-GFP localization (green, distinct foci black arrows), Nrd1-mCherry (red) and segmented cell body (orange) and nuclear envelope (cyan) indicated, slowed 200x.

Figure. 1. Single-molecule Slimfield microscopy of live cells reveals Mig1 clusters. (A) Dual-color fluorescence microscopy assay. Mig1-GFP localization change (cyan, right panels) depending on glucose availability. (B) Example Slimfield micrographs of change of Mig1-GFP localization (green) with glucose for three cells, nuclear Nrd1-mCherry indicated (red, left), mean and SEM errorbounds of total cytoplasmic (yellow) and nuclear (blue) contributions shown (lower panel), n=15 cells. Display scale fixed throughout each time course to show pool and foci fluorescence. (C) Example Slimfield micrographs of cells showing nuclear (left), trans-nuclear (center) and cytoplasmic (right) Mig1-GFP localization (green, distinct foci white arrows), Nrd1-mCherry (red) and segmented cell body (yellow) and nuclear envelope (blue) indicated. Display scales adjusted to only show foci. (D) Kernel density estimations (KDE) for Mig1-GFP content in pool and foci for cytoplasm and nucleus at *glucose* (+/-), n=30 cells.

Figure. 1 – Figure Supplement 1. Brightfield and fluorescence micrographs of key strains and glucose conditions.

Representative Slimfield fluorescence images obtained from the strains and different extracellular glucose conditions used in this study. Brightfield non-fluorescence images, segmentation perimeter indicated for cell body (orange) and nucleus (cyan), and fluorescence images are indicated, the latter showing both green and red channels obtained as the frame average from the first five consecutive Slimfield images. Fluorescence images are of the first illuminated frame and are all normalized by total pixel intensity. Snf1AS represents an ATP analog sensitive version of Snf1, Snf1-I132G. For the Mig1-mEos2 strain (inset, bottom right) this shows the brightfield image (left panel), a 300 consecutive frame average from the red channel after photoconversion (middle panel) and super-resolution false color heat map reconstruction, 40nm lateral resolution, >2,000 localizations (right panel).

Figure. 1 - Figure Supplement 2. Fluorescent reporter strains have similar viability to wild type, with relatively fast maturation of fluorescent protein, and no evidence for GFP-mediated oligomerization. (A) (left panel) Mean doubling time \pm SEM, number of cultures n=6; (right panel) relative expression of *MIG1* to constitutive *ACT1* using qPCR in the wild type and Mig1-mGFP in cells pre-grown in elevated (4%) and depleted (0.2%) glucose, SD error bars, n=3 repeats for each. (B) ‘Monomeric’ mGFP (red) vs Standard enhanced eGFP (blue) *in vitro* intensity KDE distributions. GFP/mCherry maturation. n=1000 foci (C) After continuous illumination images were taken at subsequent time intervals. To prevent appearance of newly synthesized fluorescent proteins, 100 μ g/ml cycloheximide was added 1h prior to photobleaching. Upper panels represent autofluorescence appearance in green and red channels in BY4741 wild type cells. Standard epifluorescence images (green/red) overlaid on brightfield (gray). (D) GFP and mCherry maturation in minimal YNB media with complete amino acid supplement and 4% glucose. The background-corrected total cellular fluorescence intensity for the wild type (autofluorescence) and Mig1-GFP:Nrd1-mCherry strain was quantified at each time point for each cell in ImageJ. Error bars indicate SEM. (E) and (F) *In vivo* Mig1-GFP vs Mig1-mGFP stoichiometry KDE distributions compared in *glucose* (+) and *glucose* (-) respectively ($\chi^2=0.28$, $p=1 \times 10^{-132}$ and $\chi^2=0.011$, $p=3 \times 10^{-216}$). n=30 cells.

Figure. 1 - Figure Supplement 3. *In vivo* Mig1-GFP foci intensity traces as a function of time. Showing the raw tracked intensity (blue line) and filtered (red squares) using an edge preserving Chung-Kennedy filter (88, 89) (15ms window) for (A) nuclear foci (B) cytoplasmic foci and (C) overtracked foci from >0.5s into the photobleach with steps at single GFP intensity. (D) The intensity distribution of Mig1-GFP *in vivo* at glucose (+/-) using kernel density estimate. Mode values are identical within error: 5200 ± 1500 , 4600 ± 700 respectively.

Figure. 2. Mig1 foci stoichiometry, mobility and localization depend on glucose. Heat map showing dependence of stoichiometry of detected GFP-labeled Mig1 foci with D under (A) glucose (+) and (B) glucose (-) extracellular conditions. Mean values for glucose (+) nuclear and glucose (-) cytoplasmic foci indicated (arrows). $n=30$ cells. Heat maps generated using 1,000 square pixel grid and 15 pixel width Gaussians at each foci, using variable color scales specified by colorbar on the right.

Figure. 2 – Figure Supplement 1. Mig1 phosphorylation does not affect clustering but regulates localization. Heat maps showing dependence of stoichiometry of detected GFP-labeled Mig1 foci with D in (A, B) *SNF1* deletion strain, (C) strain with ATP analog sensitive variant of Snf1, Snf1-I132G, in presence of 1NM-PP1, and (D, E) strain with four serine phosphorylation sites of Mig1 mutated to alanine.

Figure. 2 – Figure Supplement 2. Wild type Snf1 and analog sensitive have similar effect on Mig1. (A) Representative Slimfield fluorescence images showing expected Mig1 localization for a strain carrying an analog sensitive Snf1 and upon treatment with DMSO. (B, C) Heat maps showing dependence of stoichiometry of detected GFP-labeled Mig1 foci with microscopic diffusion coefficient D in analog sensitive Snf1.

Figure. 2 – Figure Supplement 3. Boxplot summary of wild type and mutant Mig1 stoichiometry and microscopic diffusion coefficient. Boxplots for stoichiometry (top) and diffusion coefficient (bottom). Median in red, quartiles in blue. Black dotted lines mark the extrema, limited to 4x and 2x upper quartile value for stoichiometry and microscopic diffusion coefficient D respectively with outliers marked with red crosses.

Figure. 3. Repressor clusters have heterogeneous mobility depending on localization. (A) Cumulative probability, glucose (+) nuclear tracks (blue) and 2 component exponential fit (red), with dual Gamma fit to D (inset) with similar parameters. (B) Mean MSD vs τ (i.e. time interval τ) from cytoplasmic (yellow), small (blue, stoichiometry ≤ 20 Mig1-GFP molecules) and large nuclear (purple, stoichiometry > 20 Mig1-GFP molecules) foci, SEM indicated, on log-log axes, $n=30$ cells for glucose (+) and (-). Anomalous diffusion model fits to time intervals ≤ 30 ms (dashed black line), anomalous coefficient $\alpha=0.4-0.8$. (C) Heat map of trans-nuclear track localizations normalized to crossover point, generated using 1000 square pixel grid and 10 pixel width Gaussians at each localization (D) distance parallel (left) and perpendicular (right) to nuclear envelope with time, normalized to crossover point for Mig1-GFP foci entering (blue) and leaving the nucleus (red), (E) dwell times at nuclear

envelope and single exponential fits (dotted). (F) Example *glucose* (+) single cell FRAP Slimfield images, fixed display scale (G) mean and SEM nuclear intensity after bleaching, n=5 and 7 cells for *glucose* (-/+), respectively.

Figure. 3 – Figure Supplement 1. Cumulative probability distance analysis reveals a single mobile population in the cytoplasm at glucose (+/-) and in the nucleus and glucose (-). Cumulative density functions of first displacement in trajectories (blue) with appropriate fits (red). Bottom right panel indicates Mig1 mutant for which the Zn finger domain has been deleted.

Figure. 4. Mig1 clusters are stabilized by depletion forces and bind to promoter targets. (A) Zoom-in on pairwise difference distribution for stoichiometry of Mig1-GFP foci, 7-mer intervals (dashed) and power spectrum (inset), mean and Gaussian sigma error (arrow). (B) Stoichiometry for Mig1-GFP clusters *in vitro* in PEG absence (blue)/presence (red). n=1000 foci. Inset shows the full range while outer zooms in on cluster stoichiometry. (C) 3C model of chromosomal DNA (blue shaded differently for each chromosome) with overlaid Mig1 promoter binding sites from bioinformatics (red), simulated image based on model with realistic signal and noise added (inset). (D) Cluster (red) and monomer (dark blue) model (goodness-of-fit $R^2 < 0$) for Mig1-GFP stoichiometry (10 replicates) compared against experimental data (cyan, $R^2 = 0.75$).

Figure. 4 – Figure Supplement 1. Additional Mig1 cluster investigations. (A) Zoom-in on pairwise difference distribution for stoichiometry of GFP-labeled Mig1 foci detected during FRAP, ~8-mer intervals (dashed lines) and power spectrum (inset) shown, mean and Gaussian sigma error (arrow). (B) GFP-labeled Mig1 cluster size as a function of stoichiometry with power law fit indicated. (C) Immuno-gold transmission electron microscopy for negatively stained 90nm cryosections of (upper panel) two different Mig1-GFP cells and (lower panel) two different Msn2-GFP cells, with zoom in (inset).

Figure. 4 – Figure Supplement 2. *In vitro* cluster characterization. (A) Native PAGE of total cell protein extracts obtained from cells grown in 4% *glucose* (+) and 0.05% *glucose* (-) conditions followed by western blotting and probing with anti-GFP antibodies. (B) Coomassie staining of purified Mig1-mGFP fraction indicates a single band that corresponds to the size of a Mig1-GFP monomer (molecular weight 83.4kDa). (C) Mig1 phosphorylation status is detected by SDS-PAGE on total cell protein extracts obtained from cells grown in different glucose conditions followed by western blotting. De/phosphorylation of Mig1 in *glucose* (+/-) respectively is not affected by the *SNF1- I132G* mutation. (D) Slimfield images of Mig1-GFP clusters *in vitro* in the absence (left) and presence of PEG (right), display intensity scaled in units of GFP per 5 pixel circular region of interest (ROI). (E) Distribution of stoichiometry for mGFP clusters *in vitro* in absence (blue)/presence (red) of PEG and the expected distribution of overlapping mGFP monomers (yellow).

Figure. 4 – Figure Supplement 3. Additional 3C modelling. (A) 3C model (blue) with overlaid bound Mig1 clusters to promoter binding sites from bioinformatics (red), and Mig1 clusters near the NE (green); (B) predicted stoichiometry distributions for GFP-labeled Mig1

foci in the nucleus at elevated extracellular glucose for a range of different binding models, including: a model which simulates both nuclear envelope (NE) translocating clusters and cluster binding to promoter targets (yellow), a model which simulates both nuclear envelope (NE) translocating monomers and monomer binding to promoter targets and DNA (blue), and a model which simulates just cluster binding to promoter targets but excludes any effects from translocating clusters (purple). These models are optimized to the experimentally determined stoichiometry distribution (cyan); (C) predicted Mig1 monomer stoichiometry distributions for Mig1 bound to promoter sites in three different orientations $\sim 10^\circ$ apart.

Figure. 5. Msn2 and Mig1 forms functional clusters colocalized to transcribed mRNA from their target genes. (A) Kernel density estimations for Msn2-GFP in pool and foci for cytoplasm and nucleus at *glucose* (+/-). (B) Heat maps showing dependence of stoichiometry and *D* of detected Msn2-GFP foci, n=30 cells. (C) Slimfield imaging on the same cell in which microfluidics is used to switch from *glucose* (+) to *glucose* (-) indicating the emergence of PP7-GFP foci at *glucose* (-) which are coincident with Mig1-mCherry foci at *glucose* (+), dependent on the Mig1 Zn finger (same intensity display scales throughout). These Mig1 and PP7 foci have a high level of colocalization as seen from (D) the distribution of the numerical overlap integral between foci in red and green channels at *glucose* (+) and *glucose* (-) respectively, peaking at ~ 0.95 . n=21 cells. (E) Two example cells showing at *glucose* (-) Msn2-mKO2 foci colocalize with PP7-GFP foci. PP7-2xGFP and Msn2-mKO2 images are frame averages of $\sim 1,000$ frames, Mig1-mCherry is a Slimfield image.

Figure. 6. Mig1 and Msn2 contain disordered sequences which may mediate cluster formation. (A) Structural prediction for Mig1; Zn finger motif (cyan), disordered sections (red) from PyMOL, beta sheet (gray), phosphorylation sites (yellow); zoom-in indicates structure of conserved Zn finger from PSI-BLAST to PDB ID: 4R2E (Wilms tumor protein, WT1). (B) DISOPRED prediction for Mig1 and Msn2; disordered regions (red), Zn finger regions (cyan). (C) Circular dichroism of Mig1-GFP *in vitro* in PEG absence (blue)/presence (orange) (D) Distribution of nearest neighbor distances for Mig1 sites within promoters on same (blue) or different (red) chromosome. (E) Schematic of depletion-stabilized Mig1 cluster bound to multiple promoter targets (Zn finger PDB ID: 4R2E). (F) Amino acid residue electrostatic charge plots for Mig1 and Msn2 from EMBOSS (90) Residues 'D' and 'E' are assigned a charge of -1, 'K' and 'R' a charge of +1, and the residue 'H' is assigned a charge of +0.5, then a rolling 75 amino acid residue window is used.

Figures and Tables

Strain name	Background	Genotype	Source/Reference
YSH1351	S288C	<i>MATa HIS3D0 LEU2D1 MET15D0 URA3D0</i>	S. Hohmann collection
YSH1703	W303-1A	<i>MATa mig1Δ::LEU2 snf1Δ::KanMX</i>	S. Hohmann collection
YSH2267	BY4741	<i>MATa his3D1 leu2D0 met15D0 ura3D0 mig1Δ::KanMX NRD1-mCherry-hphNT1</i>	S. Hohmann collection
YSH2350	BY4741	<i>MATa MSN2-GFP-HIS3 NRD1-mCherry-hphNT1 MET LYS</i>	(64)
YSH2856	BY4741	<i>MATa MIG1-eGFP-KanMX NRD1-mCherry-HphNT1 snf1Δ::LEU2 MET LYS</i>	This study
YSH2348	BY4741	<i>MATa MIG1-GFP-HIS3 NRD1-mCherry-hphNT1 MET LYS</i>	(16)
YSH2862	BY4741	<i>MATa MIG1-GFPmut3-HIS3</i>	This study
YSH2863	BY4741	<i>MATa MIG1-GFPmut3-HIS3 NRD1-mCherry-HphMX4</i>	This study
YSH2896	BY4741	<i>MATa MIG1-mEOs2-HIS3</i>	This study
ME404	BY4741	"BY4741 <i>MSN2-mKO2::LEU2 MIG1-mCherry::spHIS5 GSY1-24xPP7::KANMX msn4Δ mig2Δ nrg1::HPHMX nrg2::Met15 SUC2::NatMX</i> "	(18)
ME412	BY4741	<i>BY4741 MSN2-mKO2::LEU2 MIG1(Δaa36-91)-mCherry::spHIS5 GSY1-24xPP7::KANMX msn4Δ mig2Δnrg1::HPHMX nrg2::Met15</i>	(18)
ME411	BY4741	<i>MIG1(Δaa36-91)-mCherry::spHIS5 GSY1-24xPP7::KANMX msn4Δ mig2Δnrg1::HPHMX nrg2::Met15</i>	(18)

Plasmid name	Description	Source/Reference
pMIG1-HA	<i>HIS3</i>	(91)
pSNF1-TAP	<i>URA3, in pRS316</i>	S. Hohmann collection
pSNF1-I132G-TAP	<i>URA3, in pRS316</i>	S. Hohmann collection
pmGFPS	<i>HIS3, GFPmut3 S65G, S72A, A206K</i>	This study
pMig1-mGFP	<i>6xHIS-Mig1-GFPmut3 in pRSET A</i>	This study
pmEOs2	<i>mEOs2-HIS3 in pMK-RQ</i>	This study
YDp-L	<i>LEU2</i>	(92)
YDp-H	<i>HIS3</i>	(92)
BM3726	<i>Mig1 (Ser222,278,311,381 → Ala), URA3, in pRS316</i>	M. Johnston collection (28)
pDZ276	<i>PP7-2xGFP::URA3</i>	(18)

Table 1. *S. cerevisiae* cell strains and plasmids.

	Mig1-GFP				Msn2-GFP			
	Glucose (+)		Glucose (-)		Glucose (+)		Glucose (-)	
	Mean	SD	Mean	SD	Mean	SD	Mean	SD
Cytoplasmic Pool	509	274	949	394	1422	977	2487	1360
Nuclear Pool	77	101	140	97	551	608	1692	1221
Total Pool	586	336	1088	392	1973	1585	4179	2581
Cytoplasmic Spots	57	79	311	212	333	196	776	635
Nuclear Spots	190	99	35	63	81	138	320	269
Total Spots	246	100	345	203	414	334	1096	904
Total Cytoplasm	580	276	1156	399	1755	1173	3263	1995
Total Nuclear	226	155	176	124	632	746	2012	1490
Total Cell	806	353	1331	352	2387	1919	5274	3485

Table 2. Copy number data.

	Mig1-GFP						Msn2-GFP					
	Glucose (+)			Glucose (-)			Glucose (+)			Glucose (-)		
	Mean	SD	N	Mean	SD	N	Mean	SD	N	Mean	SD	N
Stoichiometry of Nuclear Spots	19.0	16.2	7.2	8.5	4.8	5.8	34.5	26.6	3.5	46.5	31.6	4.7
Diffusion Constant of Nuclear Spots ($\mu\text{m}^2/\text{s}$)	0.8	0.8	7.2	1.3	1.5	5.8	0.7	0.9	3.5	0.9	0.9	4.7
Stoichiometry of Trans-Nuclear Spots	10.6	10.2	1.0	8.7	5.3	5.1	21.8	16.7	1.9	43.9	35.0	0.9
Diffusion Constant of Trans-Nuclear Spots ($\mu\text{m}^2/\text{s}$)	1.3	1.2	1.0	1.5	1.6	5.1	1.5	1.2	1.9	1.1	1.1	0.9
Stoichiometry of Cytoplasmic Spots	6.6	4.9	1.1	7.2	3.7	17.8	25.7	19.5	4.8	30.1	17.5	4.0
Diffusion Constant of Cytoplasmic Spots ($\mu\text{m}^2/\text{s}$)	1.4	1.4	1.1	1.2	1.2	17.8	1.2	1.1	4.8	1.0	1.4	4.0

Table 3. Foci tracking data.

	Mig1-GFP <i>snf1Δ</i>					
	Glucose (+)			Glucose (-)		
	Mean	SD	N	Mean	SD	N
Stoichiometry of Nuclear Spots	17.5	10.9	13.2	23.5	15.4	10.9
Diffusion Constant of Nuclear Spots ($\mu\text{m}^2/\text{s}$)	1.1	1.1	13.2	0.7	0.8	10.9
Stoichiometry of Trans-Nuclear Spots	8.9	6.0	1.2	12.7	6.1	0.5
Diffusion Constant of Trans-Nuclear Spots ($\mu\text{m}^2/\text{s}$)	1.9	2.0	1.2	1.1	1.4	0.5
Stoichiometry of Cytoplasmic Spots	6.2	2.2	5.0	8.3	4.1	9.1
Diffusion Constant of Cytoplasmic Spots ($\mu\text{m}^2/\text{s}$)	1.3	1.2	5.0	1.0	1.2	9.1
Copy Numbers						
Cytoplasmic Pool	947	728	30	608	450	30
Nuclear Pool	807	398	30	611	325	30
Total Pool	1754	1127	30	1219	775	30
Cytoplasmic Spots	118	169	30	334	374	30
Nuclear Spots	162	69	30	164	71	30
Total Spots	280	238	30	498	445	30
Total Cytoplasm	1065	897	30	941	824	30
Total Nuclear	969	467	30	775	396	30
Total Cell	2034	1364	30	1717	1220	30

Table 4. *snf1Δ* foci tracking and copy number data.

Chromosome	length (bp)	N sites identified	N promoter sites
I	230218	41	1
II	813184	134	10
III	316620	52	2
IV	1531933	240	14
V	576874	109	8
VI	270161	58	4
VII	1090940	168	13
VIII	562643	92	2
IX	439888	94	8
X	745751	125	6
XI	666816	117	6
XII	1078177	194	12
XIII	924431	157	6
XIV	784333	135	3
XV	1091291	185	11
XVI	948066	163	6

Table 5. Number of potential Mig1 target promoter sites per chromosome.

Msn2:

Predicted residues: 704
 Number residues disordered: 394
 Overall percent disordered: 55.97
 Predicted disorder segment [1]-[2]
 Predicted disorder segment [16]-[33]
 Predicted disorder segment [55]-[199]
 Predicted disorder segment [222]-[249]
 Predicted disorder segment [322]-[365]
 Predicted disorder segment [410]-[428]
 Predicted disorder segment [469]-[480]
 Predicted disorder segment [510]-[549]
 Predicted disorder segment [572]-[641]
 Predicted disorder segment [660]-[667]
 Predicted disorder segment [694]-[695]
 Predicted disorder segment [699]-[704]

Number Disordered Regions: 12
 Longest Disordered Region: 145
 Average Prediction Score: 0.5577
 Average Strength= 0.8759
 Average Strength= 0.6958
 Average Strength= 0.8311
 Average Strength= 0.8237
 Average Strength= 0.8820
 Average Strength= 0.7475
 Average Strength= 0.6545
 Average Strength= 0.8040
 Average Strength= 0.9319
 Average Strength= 0.6829
 Average Strength= 0.5325
 Average Strength= 0.6783

Mig1:

Predicted residues: 504
 Number residues disordered: 372
 Overall percent disordered: 73.81
 Predicted disorder segment [1]-[12]
 Predicted disorder segment [25]-[33]
 Predicted disorder segment [77]-[171]
 Predicted disorder segment [173]-[240]
 Predicted disorder segment [242]-[249]
 Predicted disorder segment [254]-[272]
 Predicted disorder segment [292]-[310]
 Predicted disorder segment [327]-[386]
 Predicted disorder segment [423]-[504]

Number Disordered Regions: 9
 Longest Disordered Region: 95
 Average Prediction Score: 0.7008
 Average Strength= 0.8252
 Average Strength= 0.6502
 Average Strength= 0.8758
 Average Strength= 0.9051
 Average Strength= 0.5554
 Average Strength= 0.7890
 Average Strength= 0.8225
 Average Strength= 0.8355
 Average Strength= 0.9136

LacI:

Predicted residues: 360
 Number residues disordered: 149
 Overall percent disordered: 41.39
 Predicted disorder segment [1]-[4]
 Predicted disorder segment [18]-[52]
 Predicted disorder segment [55]-[81]
 Predicted disorder segment [88]-[100]
 Predicted disorder segment [186]-[187]
 Predicted disorder segment [238]-[256]
 Predicted disorder segment [258]-[258]
 Predicted disorder segment [313]-[360]

Number Disordered Regions: 8
 Longest Disordered Region: 48
 Average Prediction Score: 0.4418
 Average Strength= 0.6245
 Average Strength= 0.6710
 Average Strength= 0.7443
 Average Strength= 0.5841
 Average Strength= 0.5429
 Average Strength= 0.6208
 Average Strength= 0.5028
 Average Strength= 0.8331

Phosphorylation sites of Mig1 and Msn2 (uniprot.org, accessed February, 2016):

Mig1 Phosphorylation site	Disorder segment	Msn2 Phosphorylation site	Disorder segment
S264	[254]-[272]	S194	[55]-[199]
S278	-	S201	-
T280	-	S288	-
S302	[292]-[310]	S304	-
S311	[292]-[310]	S306	-
S314	-	S308	-
S80	[77]-[171]	S432	-
S108	[77]-[171]	S451	-
S214	[173]-[240]	S582	[572]-[641]
S218	[173]-[240]	S620	[572]-[641]
S222	[173]-[240]	S625	[572]-[641]
S303	[292]-[310]	T627	[572]-[641]
S310	[292]-[310]	S629	[572]-[641]
S350	[327]-[386]	S633	[572]-[641]
S367	[327]-[386]		
S370	[327]-[386]		
T371	[327]-[386]		
S377	[327]-[386]		
S379	[327]-[386]		
S381	[327]-[386]		
S400	-		
S402	-		
T455	[423]-[504]		

Table 6. Bioinformatics analysis for intrinsically disordered sequences.

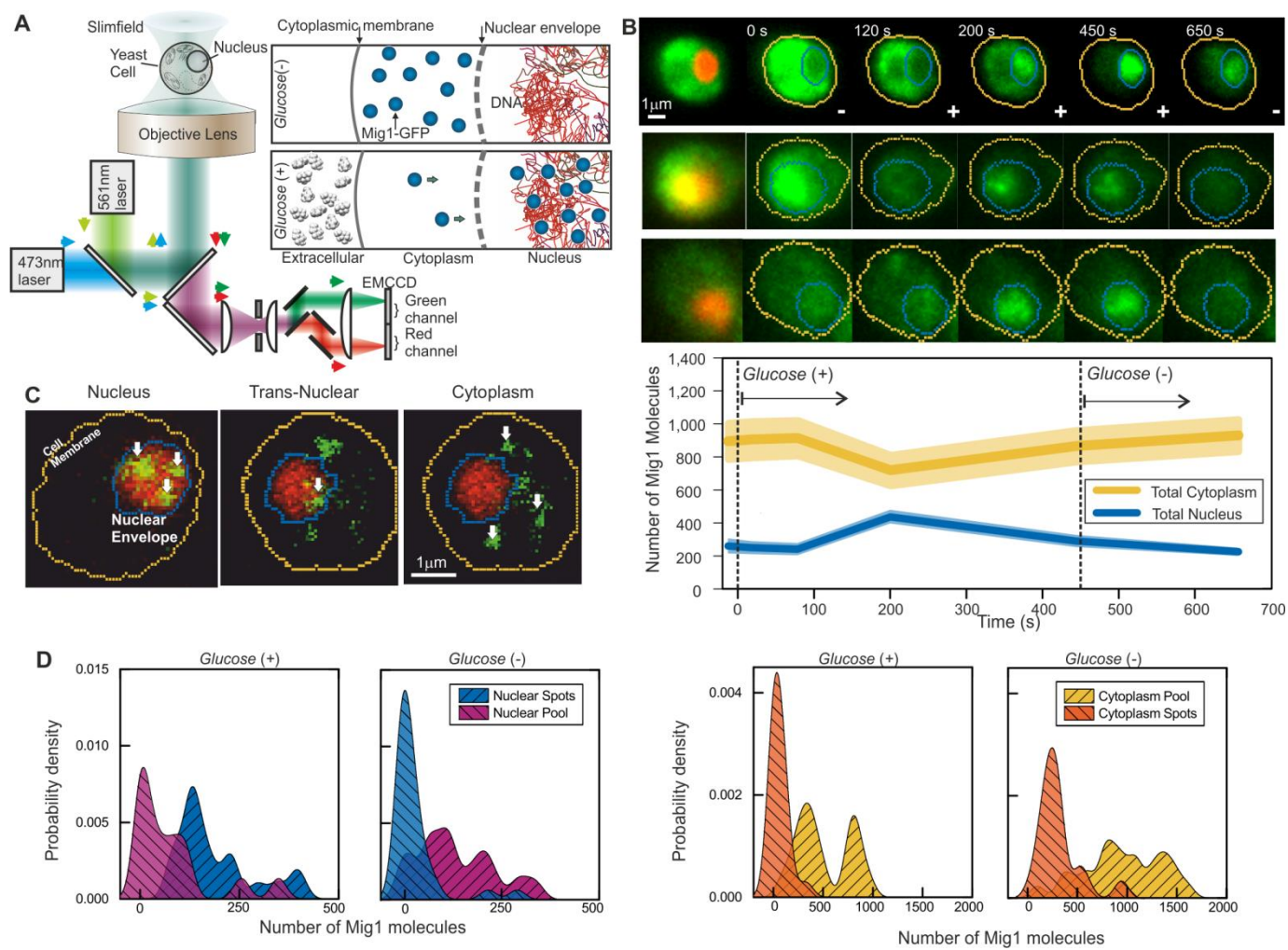


Figure. 1. Single-molecule Slimfield microscopy of live cells reveals Mig1 clusters.

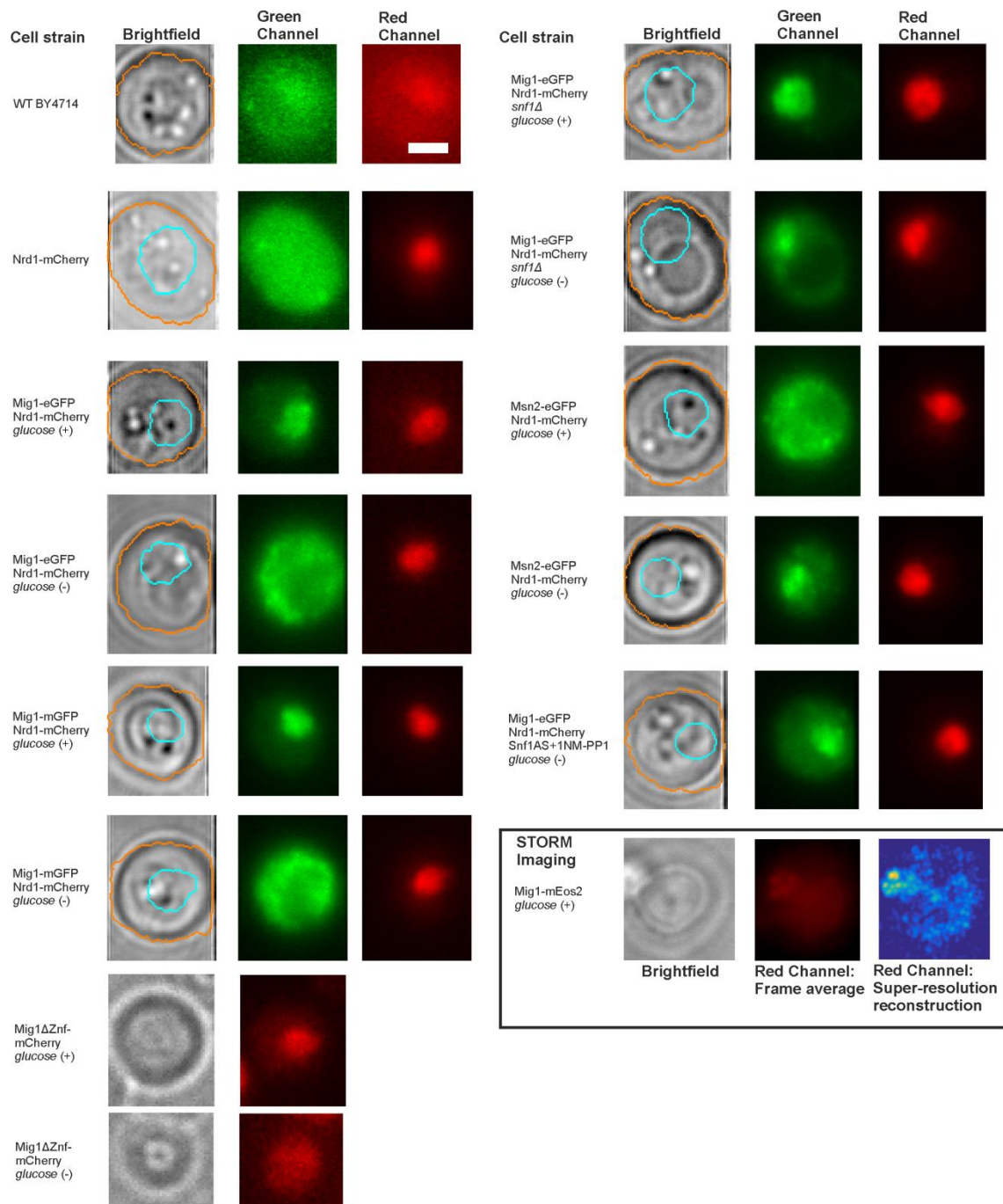


Figure. 1 – Figure Supplement 1. Brightfield and fluorescence micrographs of key strains and glucose conditions.

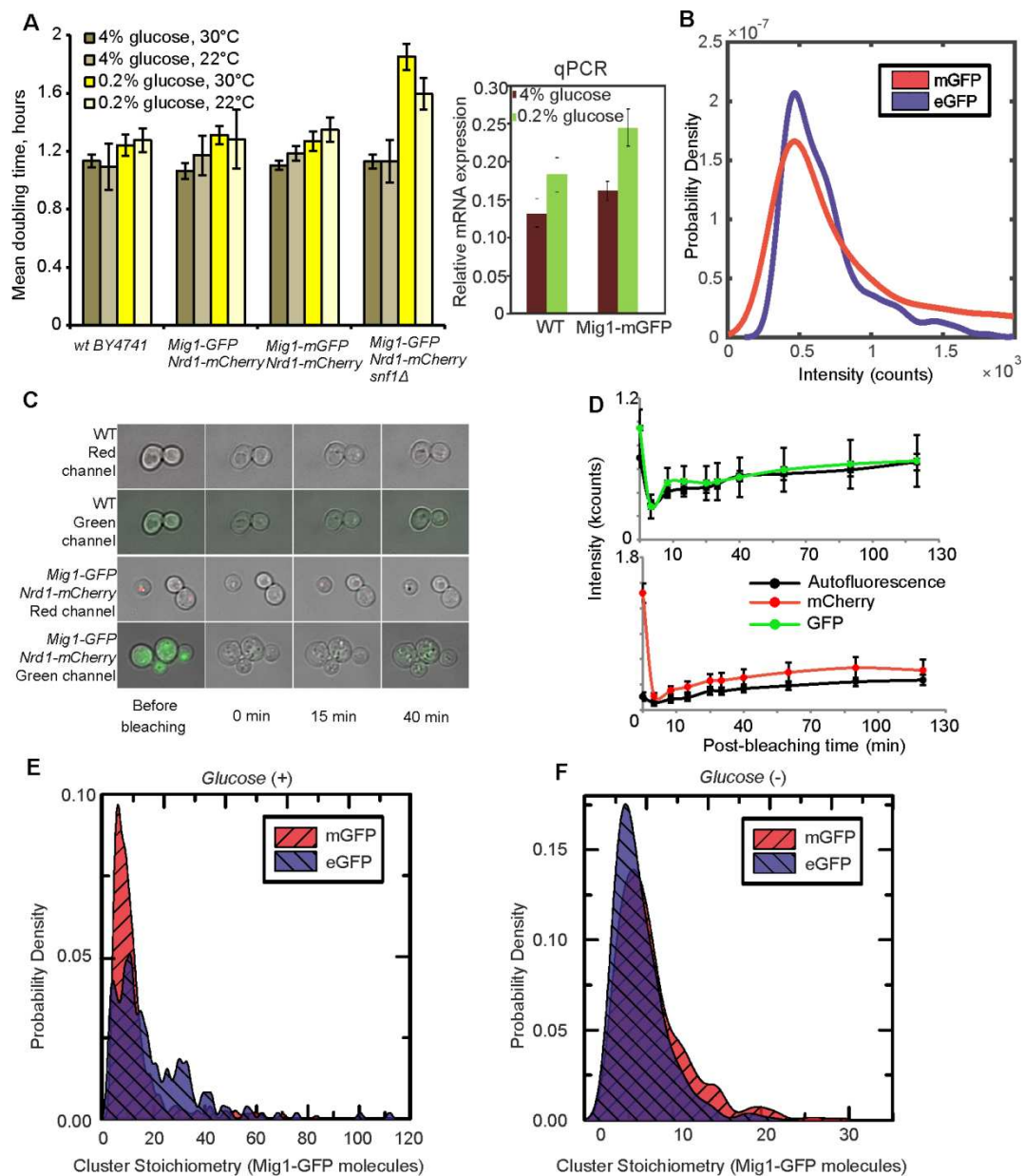


Figure 1 – Figure Supplement 2. Fluorescent reporter strains have similar viability to wild type, with relatively fast maturation of fluorescent protein, and no evidence for GFP-mediated oligomerization.

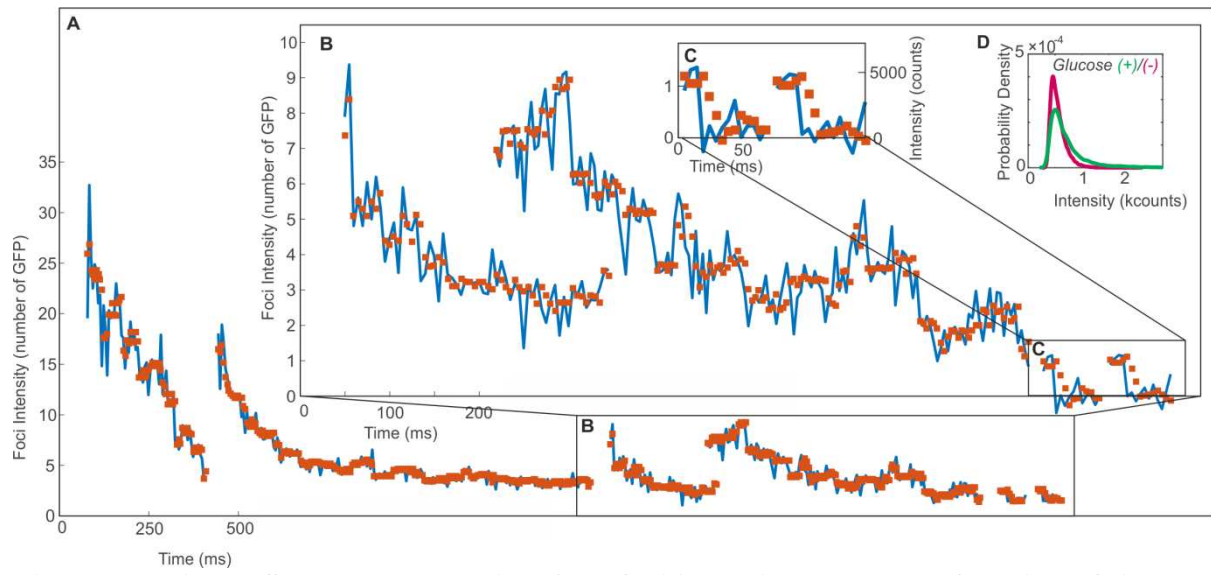


Figure. 1 - Figure Supplement 3. Mig1-GFP foci intensity traces as a function of time.

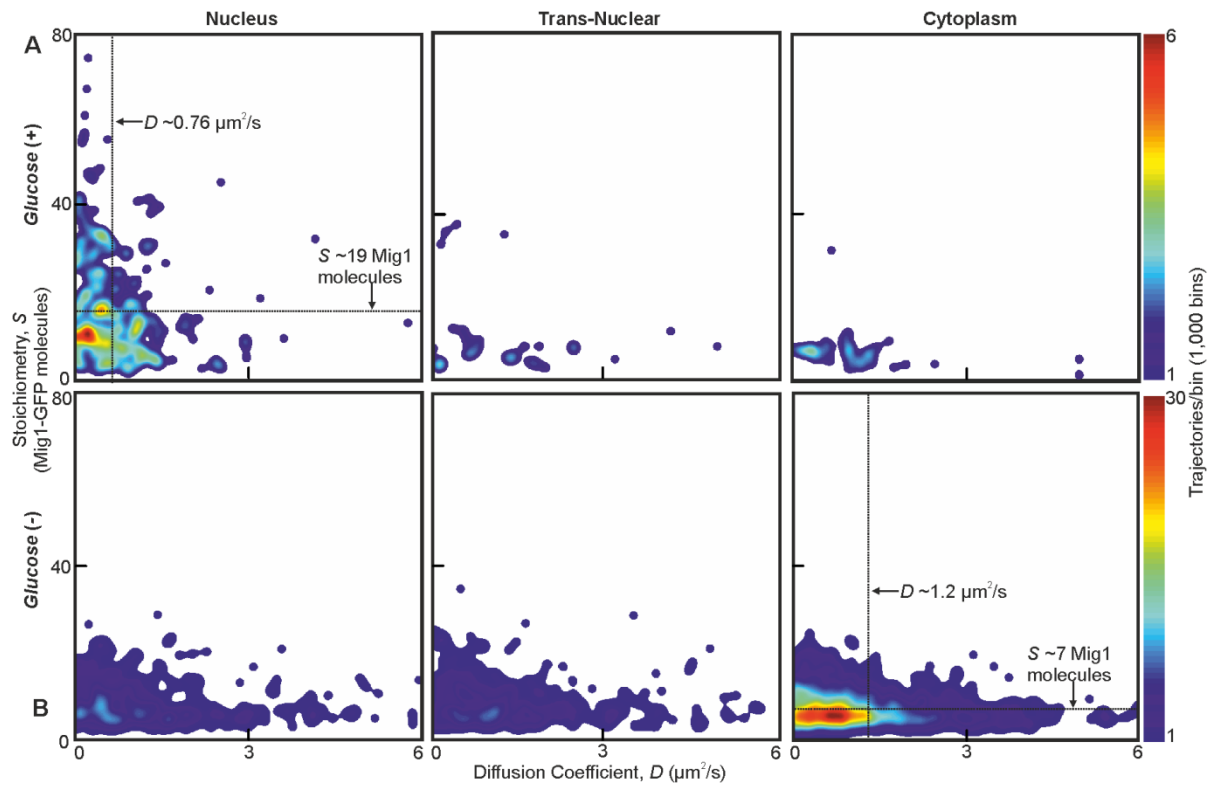


Figure. 2. Mig1 foci stoichiometry, mobility and localization depend on glucose.

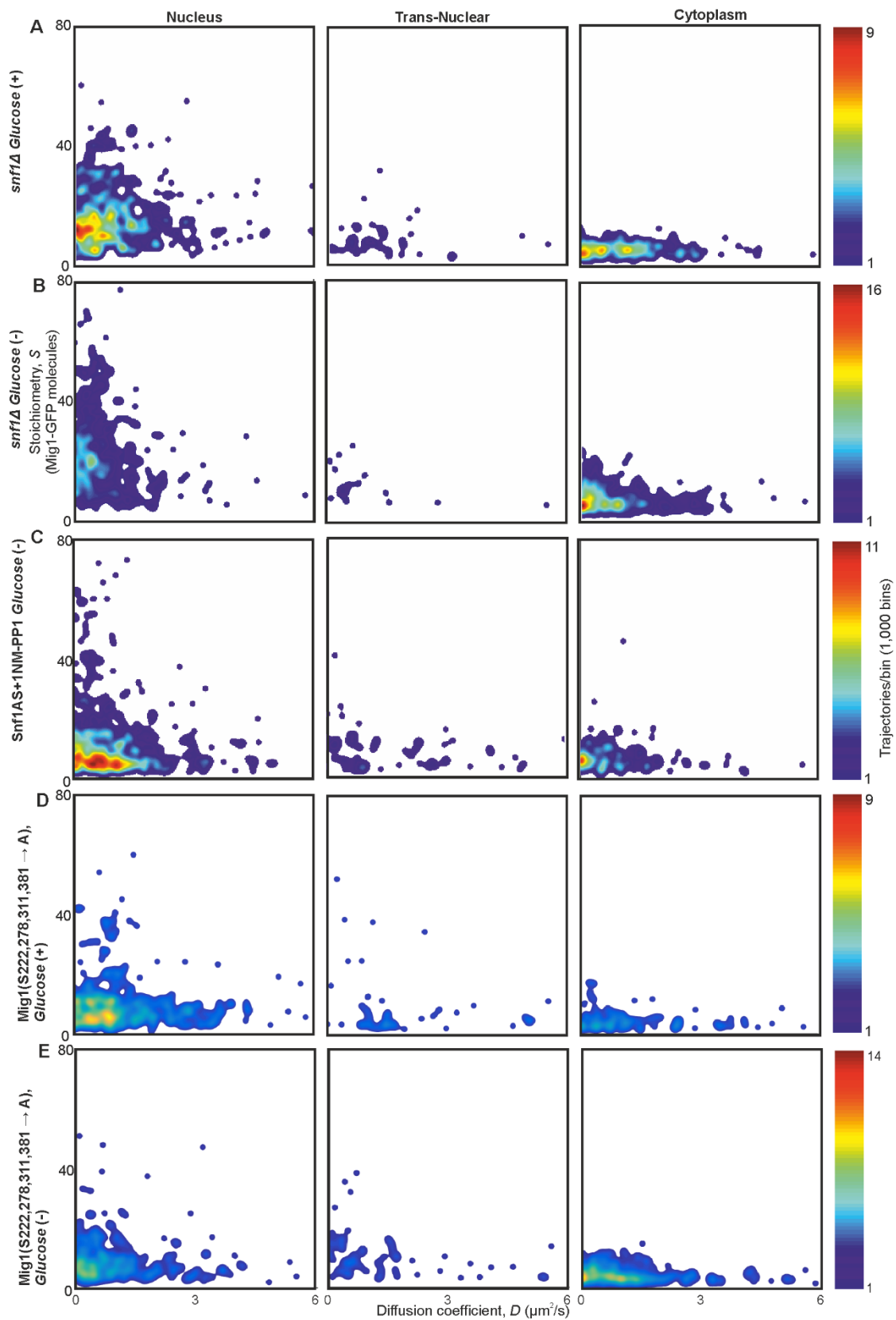


Figure. 2 – Figure Supplement 1. Mig1 phosphorylation does not affect clustering but regulates localization.

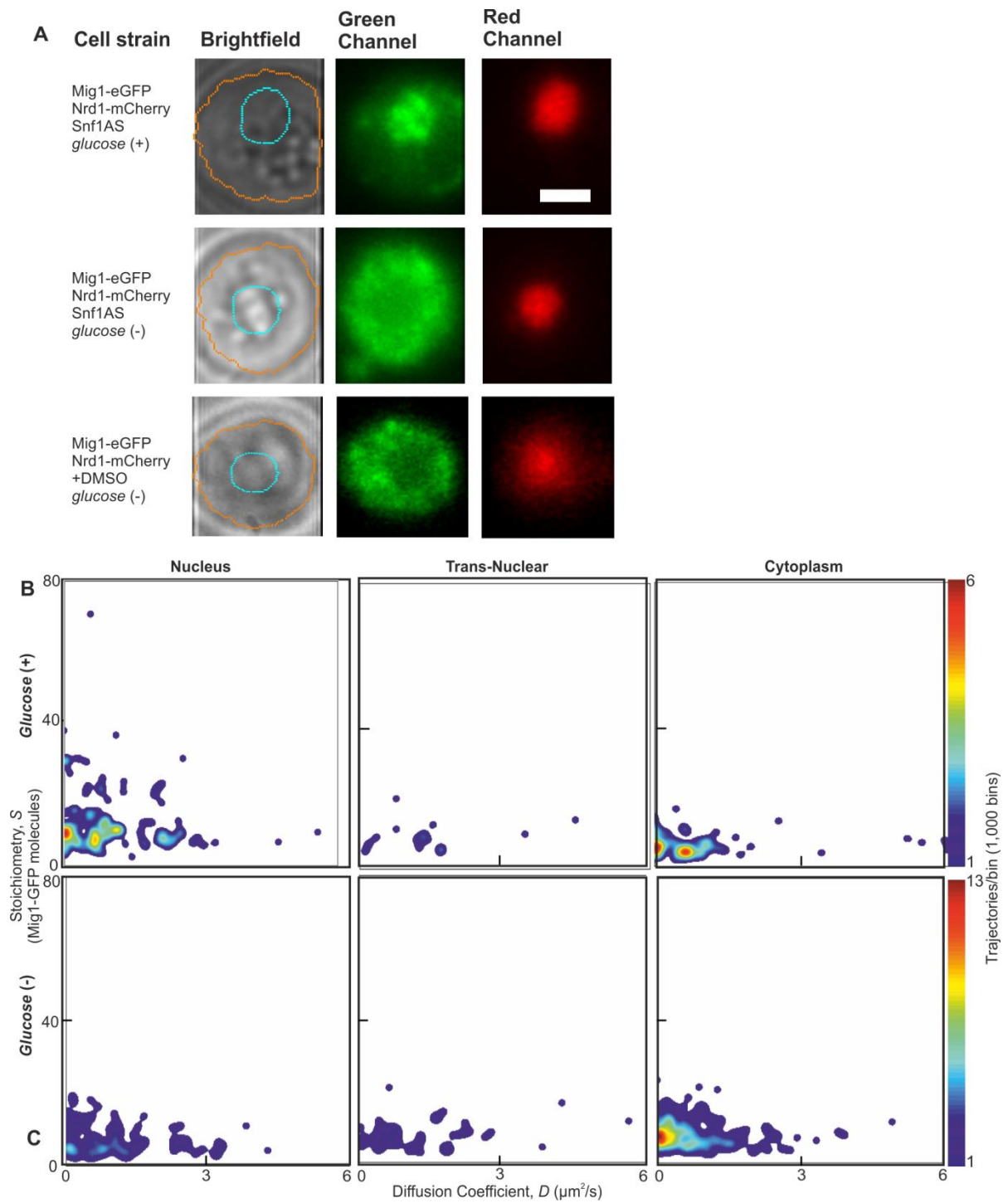


Figure. 2 – Figure Supplement 2. Wild type Snf1 and analog sensitive have similar effects on Mig1.

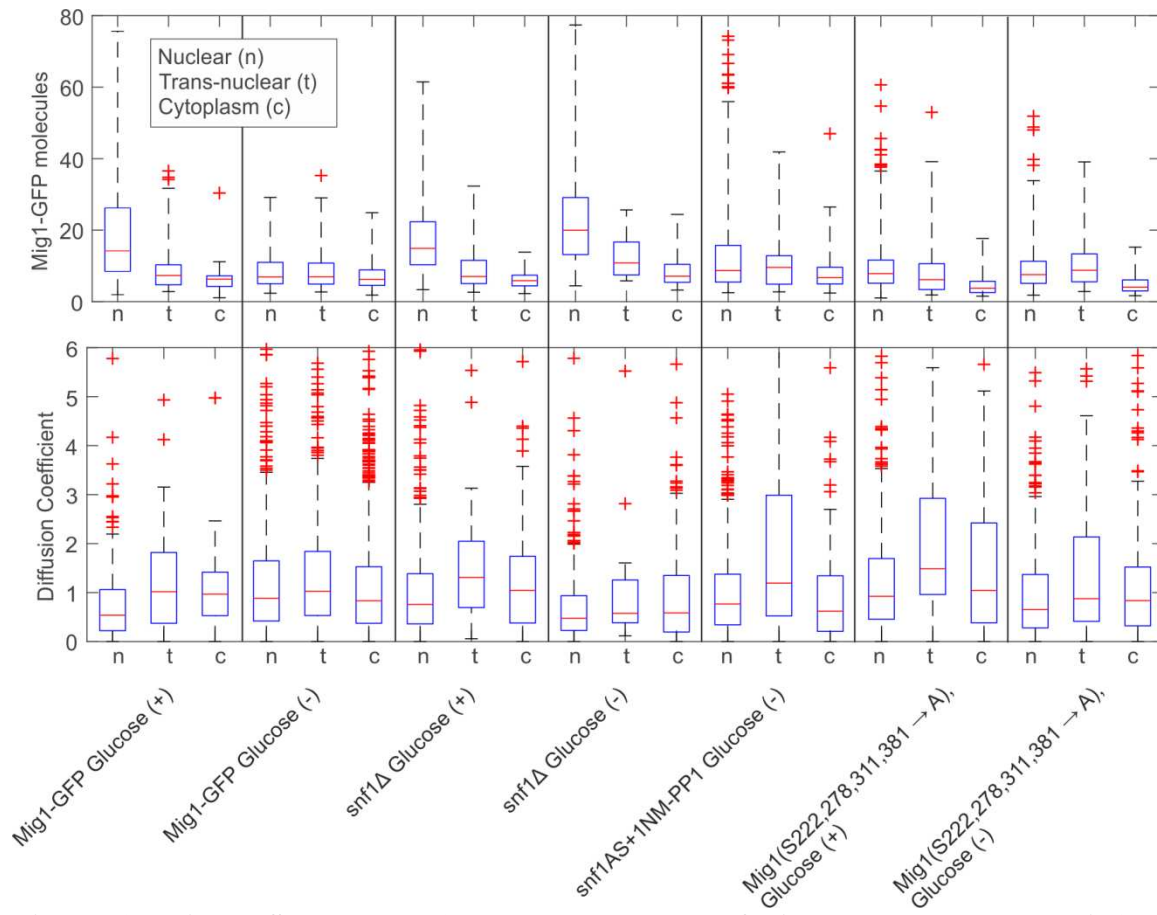


Figure. 2 – Figure Supplement 3. Boxplot summary of wild type and mutant Mig1 stoichiometry and microscopic diffusion coefficient.

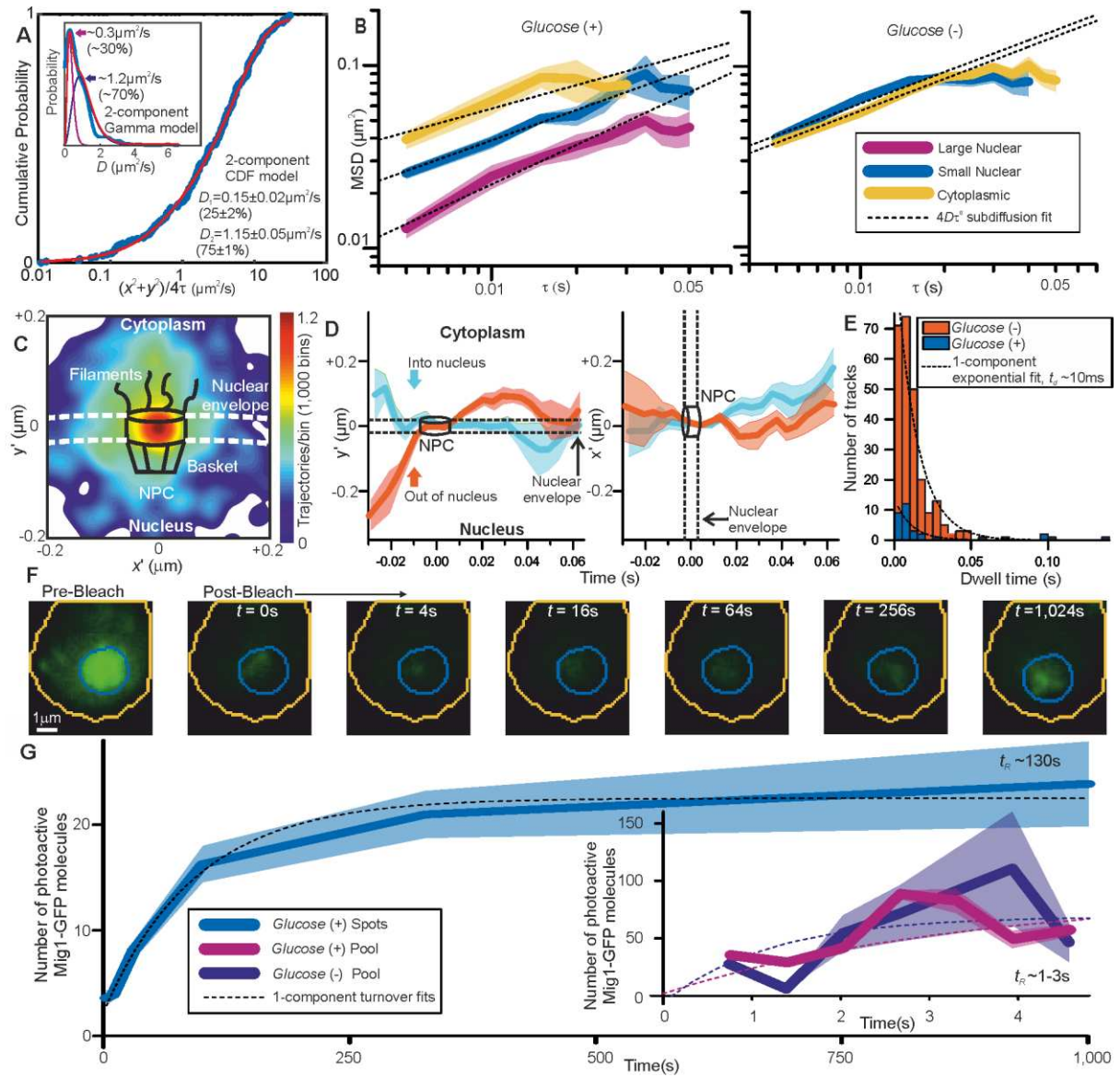


Figure 3. Repressor clusters have heterogeneous mobility depending on localization.

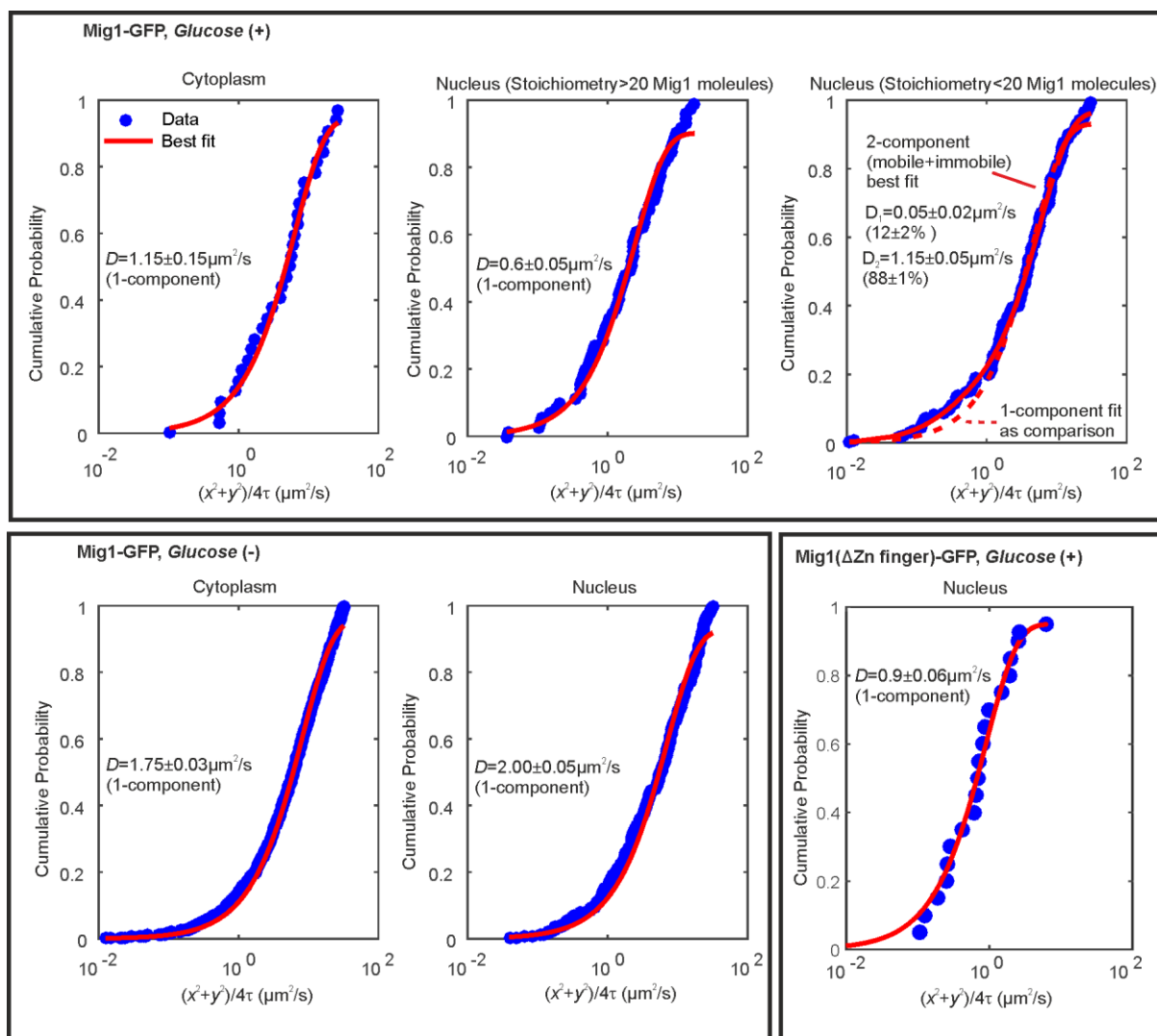


Figure. 3 – Figure Supplement 1. Cumulative probability distance analysis reveals a single mobile population in the cytoplasm at *glucose* (+/-) and in the nucleus at *glucose* (-).

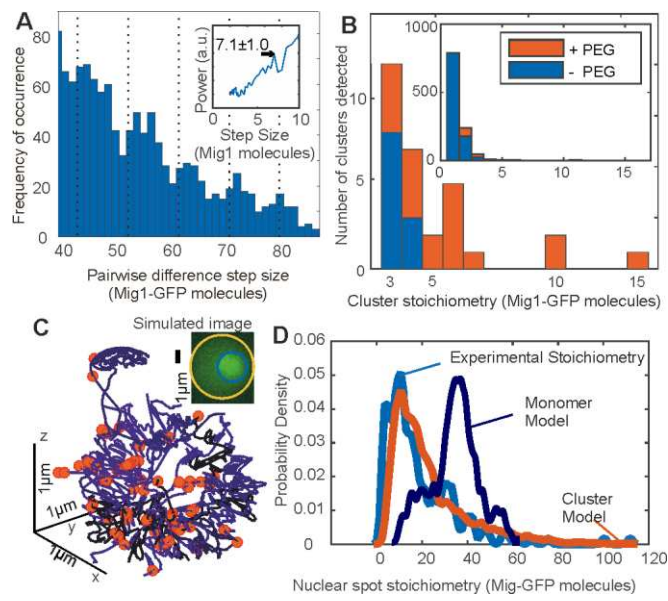


Figure. 4. Mig1 clusters are stabilized by depletion forces and bind to promoter targets.

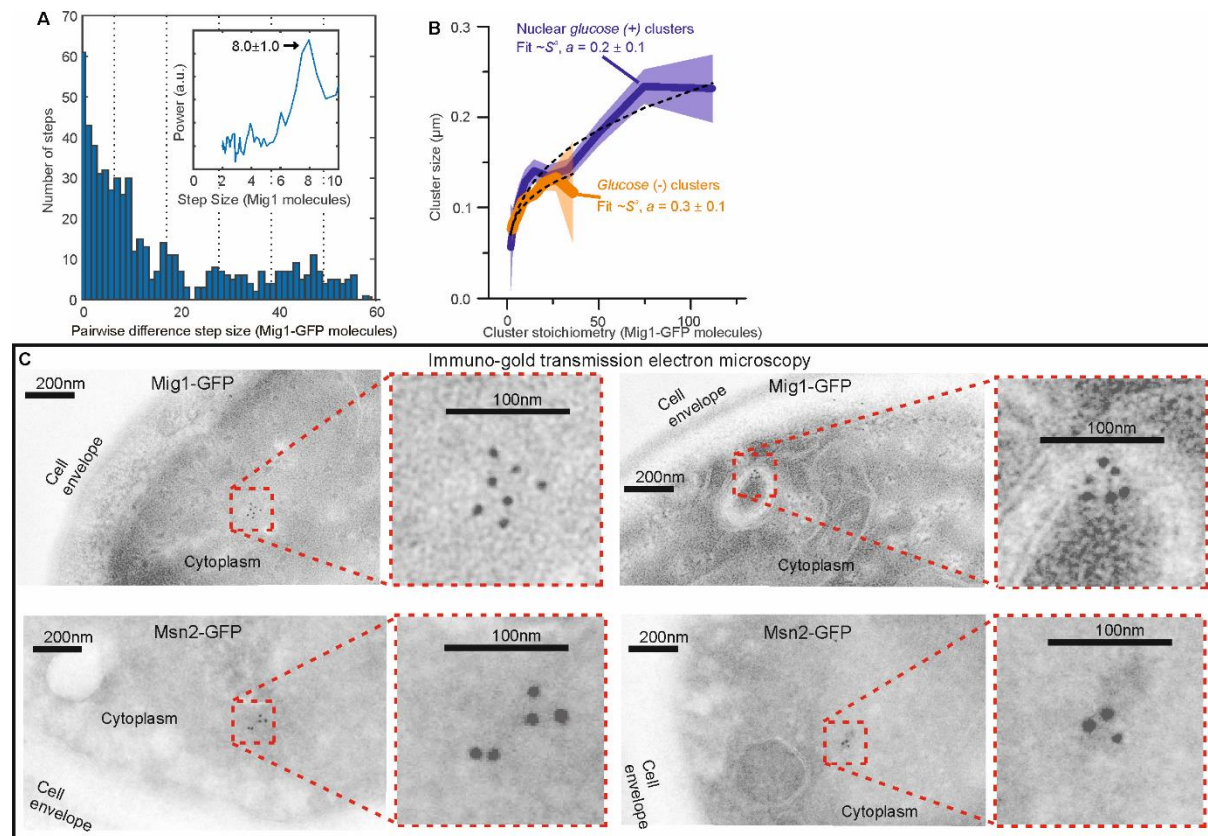


Figure. 4 – Figure Supplement 1. Additional Mig1 cluster investigations.

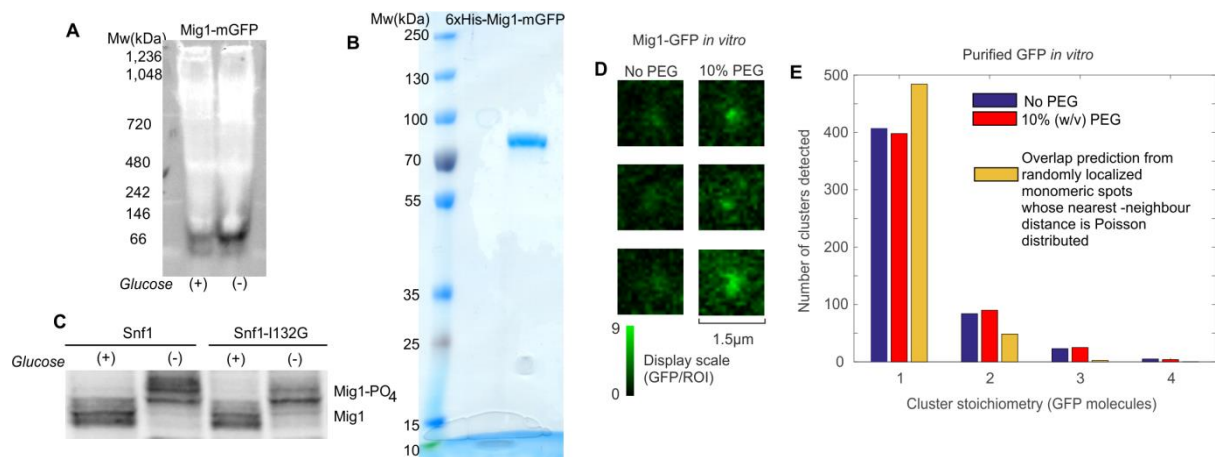


Figure. 4 – Figure Supplement 2. *In vitro* cluster characterization.

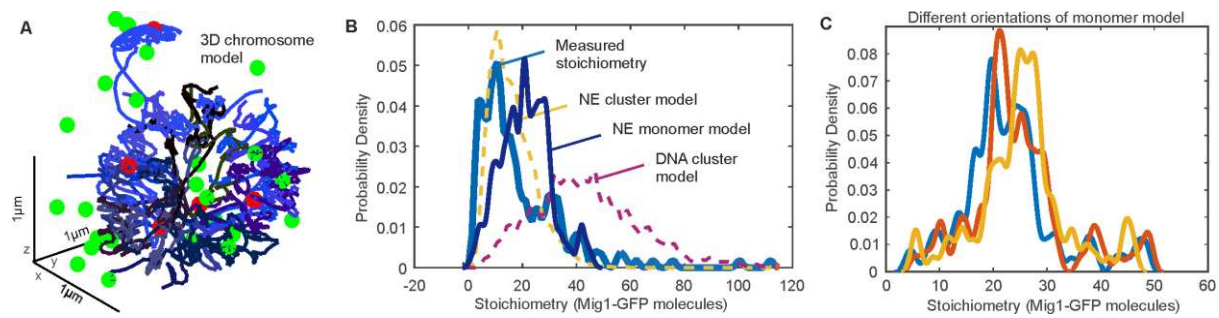


Figure. 4 – Figure Supplement 3. Additional 3C modelling.

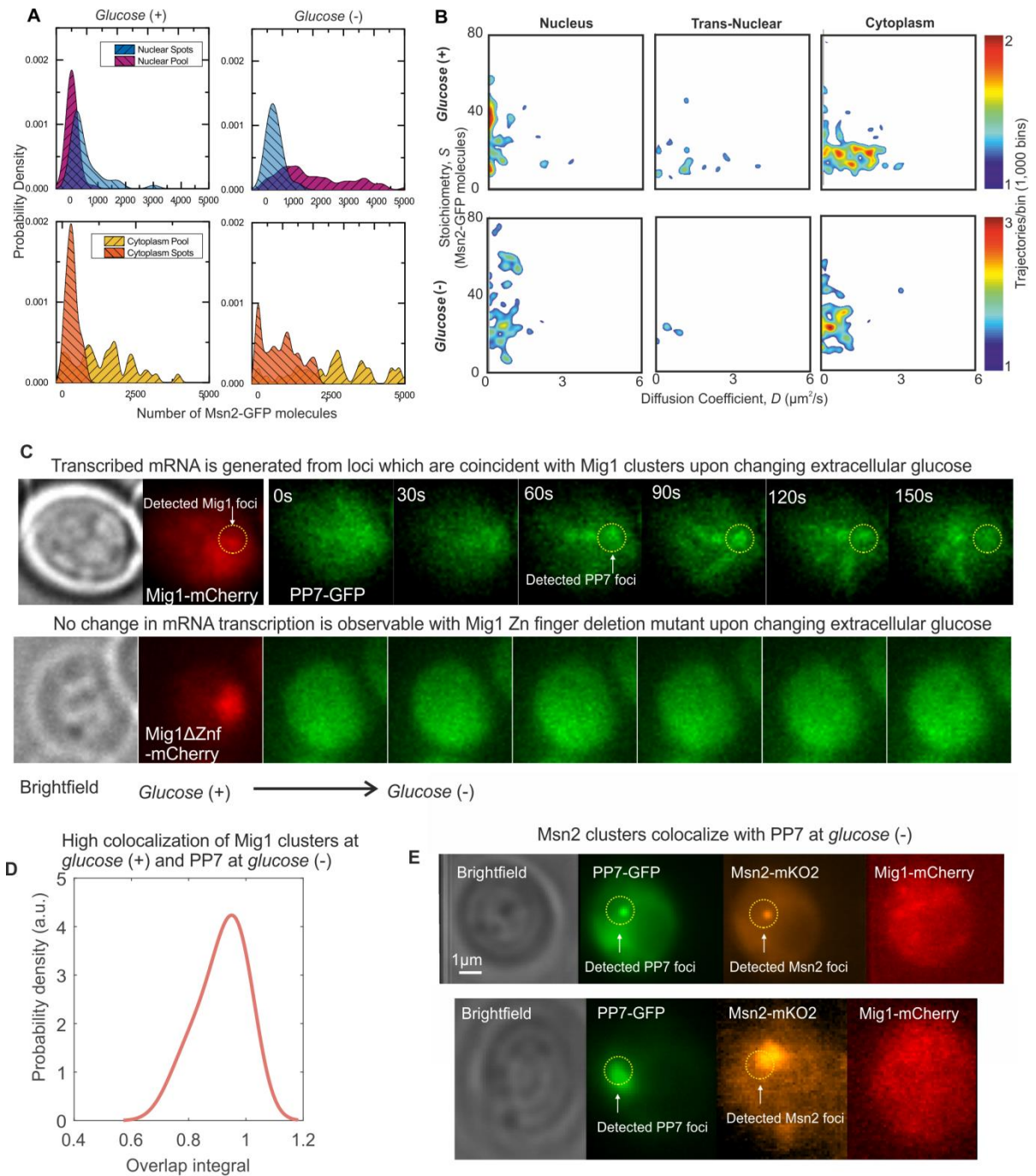


Figure. 5. Msn2 and Mig1 forms functional clusters colocalized to transcribed mRNA from their target genes

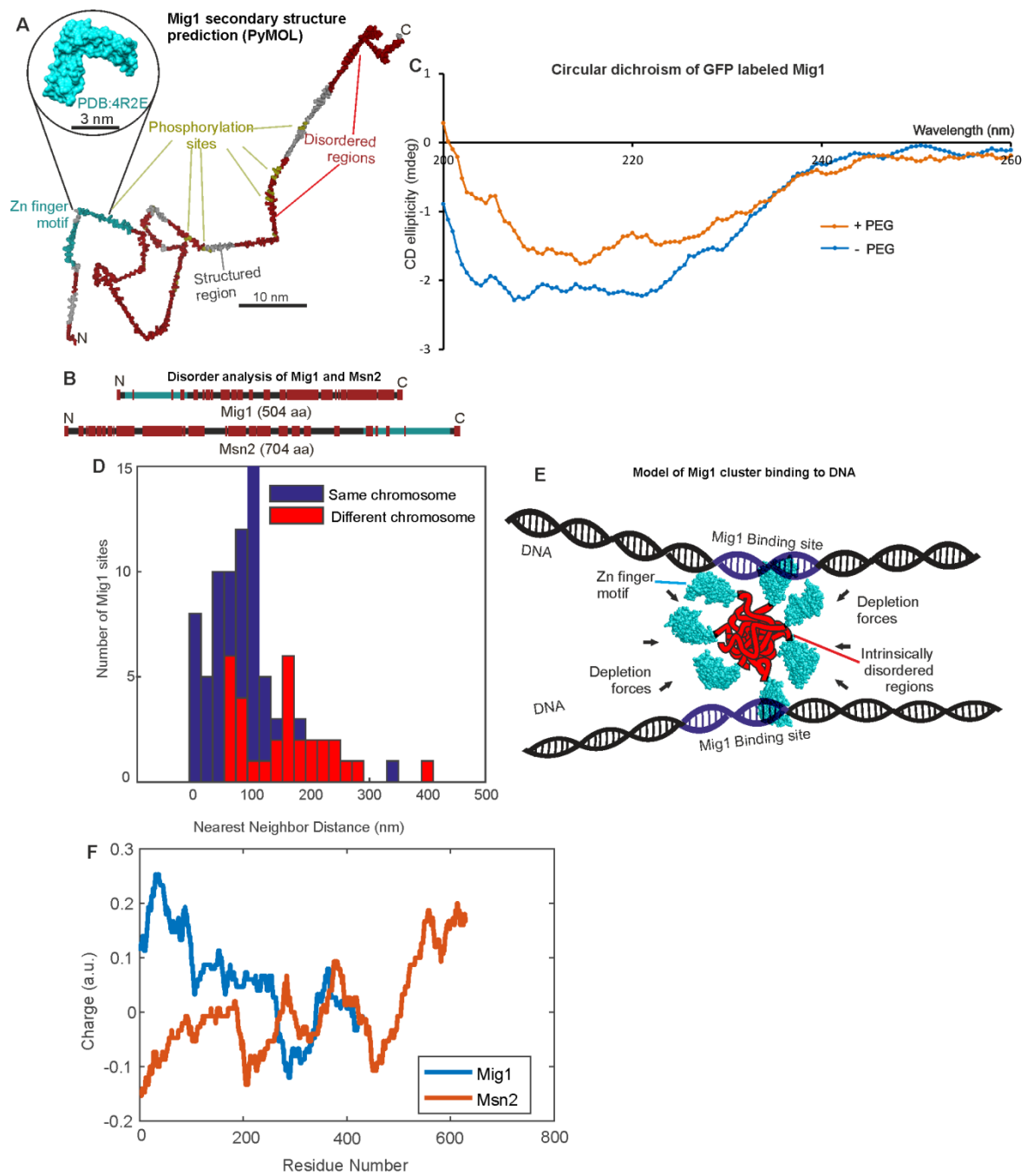


Figure. 6. Mig1 and Msn2 contain disordered sequences which may mediate cluster formation.